KCC2 Regulates Neuronal Excitability and Hippocampal Activity via Interaction with Task-3 Channels

Marie Goutierre, Sana Al Awabdh, Florian Donneger, Emeline François,
Daniel Gomez-Dominguez, Theano Irinopoulou, Liset Menendez de La Prida,
Jean Christophe Poncer

KCC2 Regulates Neuronal Excitability and Hippocampal Activity via Interaction with Task-3 Channels

Graphical Abstract
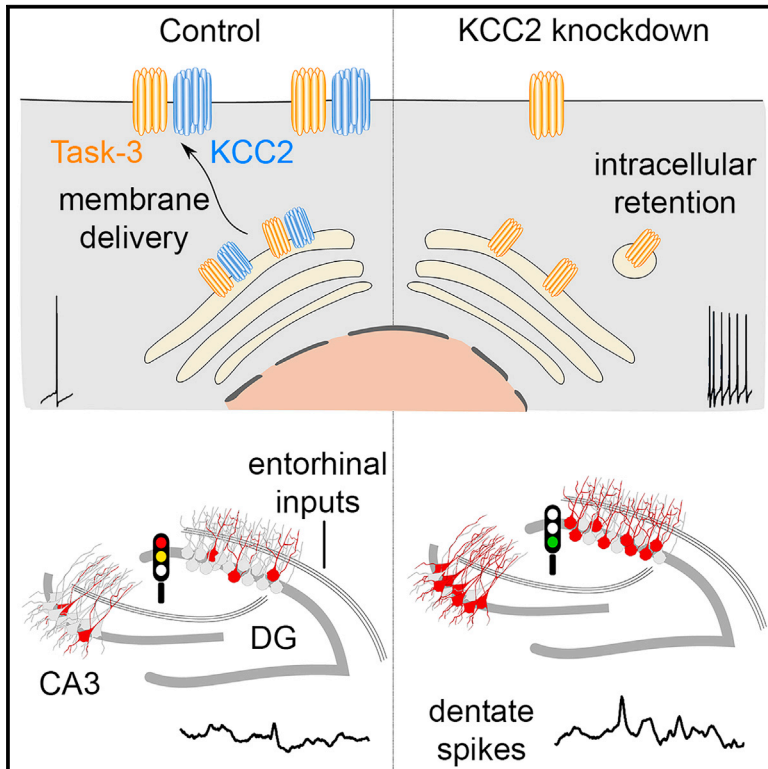
Authors

Marie Goutierre, Sana Al Awabdh, Florian Donneger, ..., Theano Irinopoulou, Liset Menendez de la Prida, Jean Christophe Poncer

Correspondence

jean-christophe.poncer@inserm.fr

In Brief

Reduced KCC2 expression is associated with numerous neurological and psychiatric disorders and assumed to primarily affect GABA signaling. Goutierre et al. demonstrate chronic KCC2 knockdown in rat hippocampus has little effect on GABA signaling but affects neuronal excitability and network activity by downregulating membrane expression of Task-3 leak potassium channels.

Highlights

- KCC2 interacts with Task-3 potassium channels and regulates their membrane traffic

- KCC2 knockdown depolarizes rat hippocampal neurons and increases their excitability

- Chronic KCC2 knockdown in rat dentate gyrus is not sufficient to induce seizures

- Network activity is altered by KCC2 knockdown, mostly independent of GABA signaling

CellPress

KCC2 Regulates Neuronal Excitability and Hippocampal Activity via Interaction with Task-3 Channels

Marie Goutierre,[1,2,3] Sana Al Awabdh,[1,2,3] Florian Donneger,[1,2,3] Emeline François,[1,2,3] Daniel Gomez-Dominguez,[4] Theano Irinopoulou,[1,2,3] Liset Menendez de la Prida,[4] and Jean Christophe Poncer[1,2,3,5,*]
[1]INSERM UMR-S 1270, 75005 Paris, France
[2]Sorbonne Université, 75005 Paris, France
[3]Institut du Fer à Moulin, 75005 Paris, France
[4]Instituto Cajal, Consejo Superior de Investigaciones Científicas (CSIC), Madrid 28002, Spain
[5]Lead Contact
*Correspondence: jean-christophe.poncer@inserm.fr
https://doi.org/10.1016/j.celrep.2019.06.001

SUMMARY

KCC2 regulates neuronal transmembrane chloride gradients and thereby controls GABA signaling in the brain. KCC2 downregulation is observed in numerous neurological and psychiatric disorders. Paradoxical, excitatory GABA signaling is usually assumed to contribute to abnormal network activity underlying the pathology. We tested this hypothesis and explored the functional impact of chronic KCC2 downregulation in the rat dentate gyrus. Although the reversal potential of GABAA receptor currents is depolarized in KCC2 knockdown neurons, this shift is compensated by depolarization of the resting membrane potential. This reflects downregulation of leak potassium currents. We show KCC2 interacts with Task-3 (KCNK9) channels and is required for their membrane expression. Increased neuronal excitability upon KCC2 suppression altered dentate gyrus rhythmogenesis, which could be normalized by chemogenetic hyperpolarization. Our data reveal KCC2 downregulation engages complex synaptic and cellular alterations beyond GABA signaling that perturb network activity thus offering additional targets for therapeutic intervention.

INTRODUCTION

Fast synaptic inhibition in the brain is primarily mediated by GABAA receptors (GABAAR), which are ligand-gated receptors associated with an anion-permeable conductance. GABAAR currents are carried by chloride and, to a lesser extent, bicarbonate fluxes (Bormann et al., 1987). Consequently, the net ion flux through GABAAR channels relies on both the transmembrane gradients of these ions and the neuronal resting membrane potential, which determine the driving force of GABAAR currents. In mature neurons, transmembrane chloride gradients are predominantly regulated by the opposing actions of two cation-chloride cotransporters (CCCs), KCC2 and NKCC1, which

respectively mediate outward and inward cotransport of chloride and potassium ions under basal conditions (Blaesse et al., 2009). Thus, postnatal upregulation of KCC2 expression is associated with a progressive hyperpolarizing shift in the reversal potential of GABAAR-mediated currents (E_{GABA}) (Rivera et al., 1999).

In mature neurons, KCC2 expression and function are rapidly regulated by neuronal activity via multiple posttranslational mechanisms (Côme et al., 2019; Medina et al., 2014). Thus, Ca^{2+} influx through postsynaptic NMDA receptors or during prolonged postsynaptic firing (Fiumelli et al., 2005) rapidly reduces KCC2 membrane expression and function through protein-phosphatase-1-dependent dephosphorylation of its Ser940 residue and protein cleavage by the calcium-activated protease calpain (Chamma et al., 2013; Lee et al., 2011; Puskarjov et al., 2012). Conversely, Cl^- influx through GABAA receptors stabilizes KCC2 at the plasma membrane via chloride-mediated inhibition of the serine-threonine WNK1 kinase and its downstream effectors SPAK-OSR1, which phosphorylate KCC2 on Thr906 and Thr1007 residues (Caraiscos et al., 2004; Heubl et al., 2017; Kahle et al., 2016). Finally, KCC2 expression is also regulated by several neuromodulators acting on G-protein-coupled receptors (Mahadevan and Woodin, 2016) as well as neurotrophins, such as brain-derived neurotrophic factor (BDNF), acting via TrkB signaling (Rivera et al., 2002).

KCC2 dysregulation has been associated with numerous neurological and psychiatric disorders (Kaila et al., 2014; Kahle et al., 2008). These include epilepsy (Di Cristo et al., 2018), neuropathic pain (Coull et al., 2003; Gagnon et al., 2013), post-traumatic spasticity (Boulenguez et al., 2010), Huntington disease (Dargaei et al., 2018), schizophrenia (Hyde et al., 2011), and Rett syndrome (Deidda et al., 2015; Banerjee et al., 2016; Tang et al., 2016). In most cases, reduced KCC2 expression was associated with a depolarized E_{GABA} that could be partly rescued using NKCC1 antagonists or KCC2 enhancers (Banerjee et al., 2016; Dargaei et al., 2018; Gagnon et al., 2013; Huberfeld et al., 2007; Liabeuf et al., 2017). Because these drugs also ameliorated the pathological symptoms, those were generally assumed to primarily reflect a defect in neuronal chloride transport and altered GABAergic neurotransmission.

However, KCC2 functions in neurons extend beyond the mere control of chloride transport. Through interactions with multiple

transmembrane and intracellular partners, KCC2 regulates dendritic spine morphology (Gauvain et al., 2011; Li et al., 2007) and actin cytoskeleton (Chevy et al., 2015; Llano et al., 2015), as well as the strength and long-term plasticity of glutamatergic synapses (Chevy et al., 2015; Gauvain et al., 2011). Functional proteomics data revealed additional putative KCC2 partners, including some involved in the recycling and trafficking of various transmembrane proteins and receptors (Mahadevan et al., 2017). Those may then either influence KCC2 function or, conversely, be regulated by KCC2. Thus, dysregulation of KCC2 expression may affect neuronal intrinsic and synaptic properties and thereby contribute to abnormal activity patterns that underlie neurological and psychiatric disorders. Deciphering the relative contribution of these perturbations upon KCC2 downregulation may then help predict the most effective rescue strategies.

Here, we explored the functional impact of chronic KCC2 downregulation in the rat dentate gyrus at the cellular, synaptic, and network activity levels. KCC2 knockdown had no significant effect on the driving force of GABAAR currents at rest but instead enhanced neuronal excitability and excitatory postsynaptic potential (EPSP)/spike coupling through membrane depolarization and increased resistance. Pharmacological and biochemical evidence suggest this effect primarily reflected the downregulation of a leak potassium conductance carried by tandem of pore domain in a weak inwardly rectifying K+ channels (TWIK)-related acid-sensitive 3 (Task-3) channels, the membrane expression and function of which were regulated via interaction with KCC2. KCC2 knockdown in about 40%–70% granule cells was not sufficient to promote epileptiform activity but altered dentate gyrus network activity, which was normalized by restoring granule cell membrane properties. Our results show that KCC2 downregulation affects network activity primarily through enhanced neuronal excitability, suggesting novel targets for therapeutic intervention.

RESULTS

We investigated the impact of a chronic KCC2 suppression in the dentate gyrus using *in vivo* RNAi. Young adult rats (postnatal day 30 [P30]) were stereotaxically injected in the dorsal dentate gyrus with lentiviruses expressing previously validated (Chevy et al., 2015; Gauvain et al., 2011) KCC2-directed small hairpin RNA (shKCC2) or non-target small hairpin RNA (shNT) sequences together with GFP. KCC2 knockdown in transduced neurons was first confirmed by immunofluorescence imaging 2 weeks after *in vivo* infection (Figures 1A and 1B) and quantified by western blot analysis of primary hippocampal neurons 10 days after *in vitro* infection (Figure 1C). Next, we analyzed GABAAR-mediated transmission using gramicidin perforated-patch recordings. GABAAR-mediated currents were evoked by somatic laser uncaging of Rubi-GABA (15 μM) while varying holding potentials (Figure 1D). As expected, the reversal potential of GABAAR currents (E_{GABA}) was significantly more depolarized in KCC2 knockdown neurons (-74.2 ± 2.7 mV) compared to control granule cells (-82.0 ± 2.2 mV; t test; $t_{24} = 2.22$; p = 0.0360; Figure 1E), although their mean conductance was not significantly different (3.6 ± 0.7 versus 2.5 ± 0.4 nS; Mann-Whitney test; p = 0.32).

However, KCC2 knockdown neurons also displayed more depolarized resting membrane potential (V_{rest}; -83.6 ± 1.5 versus -89.8 ± 0.8 mV; t test; $t_{24} = 3.41$; p = 0.0023). The shift in E_{GABA} and V_{rest} was of similar magnitude such that the driving force of ion flux through GABAARs at rest was not significantly affected (9.4 ± 2.5 versus 7.8 ± 2.3 mV; t test; $t_{24} = 0.48$; p = 0.63). Additionally, neither the amplitude (14.1 ± 1.2 versus 14.8 ± 0.7 pA; Mann-Whitney; p = 0.42) or mean frequency (0.9 ± 0.1 versus 1.2 ± 0.2 Hz; Mann-Whitney; p = 0.27) of miniature inhibitory postsynaptic currents (mIPSCs) was affected by chronic KCC2 knockdown (Figures 1F and 1G). Therefore, KCC2 suppression in dentate granule cells does not significantly affect steady-state GABAergic transmission, due to an unexpected depolarizing shift in resting membrane potential.

We further explored the mechanisms underlying changes in membrane potential upon KCC2 suppression in granule cells. Whole-cell recordings from infected neurons while blocking synaptic transmission showed that depolarized resting membrane potential in KCC2 knockdown granule cells (-80.8 ± 1.6 versus -87.7 ± 1.1 mV; t test; $t_{37} = 3.45$; p = 0.0014) was accompanied by an increase in input resistance (662.7 ± 47.1 versus 513.4 ± 47.9 MΩ; t test; $t_{37} = 2.21$; p = 0.033; Figure 2A). These changes resulted in higher excitability of KCC2 knockdown neurons following current injection (Figure 2C; repeated-measures ANOVA; $F_{15,555} = 11.98$; p = 3.2×10^{-7}), and no difference was observed in action potential threshold (Figure 2D; -50.7 ± 1.9 versus -50.6 ± 1.3 mV; t test; $t_{37} = 0.06$; p = 0.95), waveform, or amplitude (89.6 ± 1.8 versus 88.3 ± 3.3 mV; Mann-Whitney; p = 0.56; Figures 2E and 2F).

Increased neuronal excitability upon KCC2 downregulation was cell autonomous because neighboring uninfected cells had similar properties in slices from animals infected with viruses expressing shNT or shKCC2 (Figure S1). In addition, acute application of the KCC2-specific antagonist VU0463271 (Delpire et al., 2012; 6 μM) for more than 30 min did not affect granule cell membrane resistance (299.0 ± 26.2 versus 356.1 ± 35.7 MΩ; $t_{30} = 1.31$; p = 0.20; Figure S1), indicating KCC2-mediated ion transport per se does not significantly contribute to input resistance. Finally, these modifications were not specific of dentate granule cells, because KCC2 knockdown in CA1 pyramidal cells also resulted in depolarized resting membrane potential (-66.6 ± 1.0 versus -72.1 ± 1.5 mV; t test; $t_{20} = 2.95$; p = 0.0079), increased input resistance (213.0 ± 25.4 versus 134.5 ± 10.2 MΩ, Mann-Whitney; p = 0.0013), and shifted input-output curve (repeated-measures ANOVA; $F_{15,300} = 11.5$; p = 0.0029; Figure S2).

Depolarized membrane potential and increased input resistance likely reflect a reduction in potassium currents operating at rest. We tested this hypothesis by recording potassium currents while blocking synaptic transmission. In KCC2 knockdown granule cells, potassium conductance was reduced (Figures 2G and 2H), particularly for outward currents, as evidenced by reduced rectification index in KCC2 knockdown versus control granule cells (0.5 ± 0.1 versus 0.8 ± 0.1; t test; $t_{37} = 3.62$; p = 0.0009; Figure 2I). This suggests that outwardly rectifying leak potassium channels might be downregulated upon KCC2 suppression. Two-pore-domain potassium channels (K2P) are a large family of leak potassium channels comprising both
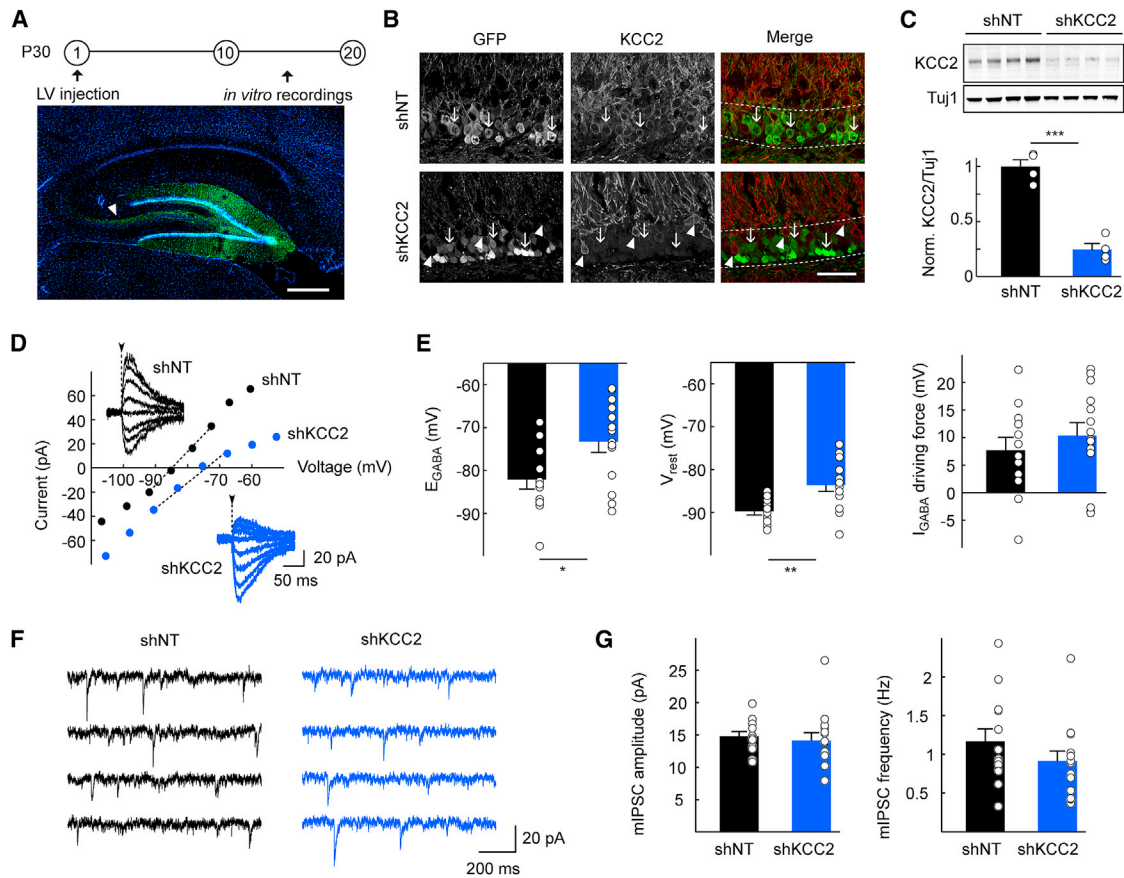
Figure 1. KCC2 Suppression in Dentate Granule Cells Does Not Alter Steady-State GABA Signaling

(A) Top: experimental timeline. Bottom: confocal micrographs show infected cells (GFP, green) and DAPI (blue) staining in a parasagittal hippocampal slice 2 weeks post-infection. Arrowhead indicates mossy fibers from infected granule cells. Scale bar, 500 μm.

(B) Confocal micrographs of infected dentate gyrus areas, showing massive extinction of KCC2 expression in KCC2 knockdown neurons. Dotted line: *st. granulosum*. Neurons expressing shNT, but not shKCC2 (arrows) show pericellular KCC2 immunostaining, as do neighboring uninfected cells (arrowheads). Scale bar, 50 μm.

(C) Western blot from 4 independent hippocampal cultures infected with the same lentiviruses (LVs) as in (A) and (B), expressing either shNT or shKCC2. Bottom: summary graph shows KCC2 immunofluorescence normalized to Tuj1.

(D) Representative currents following Rubi-GABA somatic uncaging (flash, dotted line) recorded in gramicidin perforated-patch configuration during incremental voltage steps and corresponding current-potential (I-V) curves. E_{GABA} is interpolated from the 4 points around reversal.

(E) Summary data (shNT: n = 12 cells, 6 rats; shKCC2: n = 14 cells, 6 rats) show depolarized E_{GABA} upon KCC2 suppression. The resting membrane potential (V_{rest}) is also depolarized, resulting in no significant change in the driving force of GABAergic currents. *p < 0.05; **p < 0.01; ***p < 0.001.

(F) 4-s recordings of mIPSCs from granule cells expressing shNT (black) or shKCC2 (blue).

(G) Summary data from shNT (n = 13 cells, 2 rats) and shKCC2 (n = 14 cells, 2 rats) showing no changes in mIPSCs amplitude (left; p = 0.42) or frequency (right; p = 0.27).

inward and outward rectifiers (Lesage and Lazdunski, 2000; Ketchum et al., 1995). We therefore tested whether currents carried by K2P channels may be reduced in KCC2 knockdown neurons. Bath application of bupivacaine (100 μM), a non-selective K2P channel antagonist significantly reduced potassium currents in control neurons, but not in KCC2 knockdown neurons (Figure 2G). Moreover, bupivacaine abolished the difference in resting membrane potential (-77.3 ± 1.9 versus -81.0 ± 1.5 mV; Mann-Whitney test with Bonferroni correction; p = 1; Figure 2J) and input resistance (998.7 ± 118.6 versus $1,343.1 \pm 207.4$ MΩ; Mann-Whitney test with Bonferroni correction; p = 1) between KCC2 knockdown and control granule cells. Together, these results demonstrate that chronic KCC2 sup-

pression increases neuronal excitability primarily through regulation of an outwardly rectifying leak potassium conductance.

Trek-2 and Task-3 are the most prominent outwardly rectifying K2P in dentate gyrus granule cells (Aller and Wisden, 2008; Marinc et al., 2014; Talley et al., 2001). Immunohistofluorescence imaging of Trek-2, however, revealed a predominant expression in mossy fibers (Figure S3) with little or no somato-dendritic expression, suggesting Trek-2 may not prominently contribute to granule cell resting membrane potential and membrane conductance. Conversely, Task-3 expression was primarily observed in granule cell somata and dendrites (Figure S3). We therefore examined whether Task-3 protein expression in granule cells might be affected by chronic KCC2 suppression.
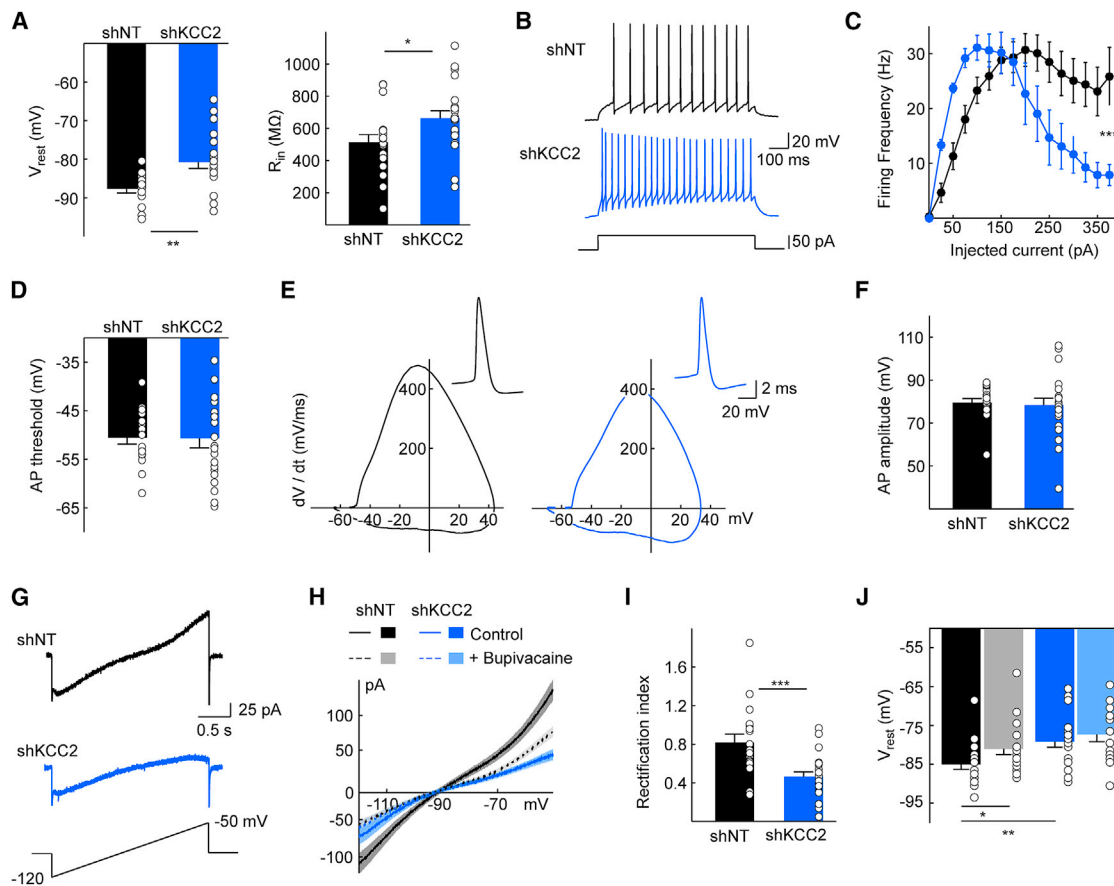
Figure 2. Increased Excitability upon KCC2 Extinction Reflects Downregulation of a Leak Potassium Conductance

(A) Summary graphs of membrane properties of granule cells expressing shNT (n = 18 cells, 5 rats) or shKCC2 (n = 21 cells, 7 rats) recorded in whole-cell patch clamp mode in the presence of synaptic transmission blockers. KCC2 knockdown resulted in depolarized membrane potential and increased input resistance.

(B) Individual traces in both conditions for a depolarizing current pulse of 50 pA.

(C) Input-output curve representing firing frequency as a function of injected current for all cells.

(D) Action potential threshold was determined as the voltage for which derivative of the signal exceeded 15 mV/ms and was not different between conditions.

(E) Individual phase plots of action potentials (insets), showing no change upon KCC2 suppression.

(F) The amplitude of action potentials was also unchanged in KCC2-knockdown cells.

(G) Representative potassium currents recorded during a voltage ramp in the presence of synaptic transmission blockers and TTX.

(H) Summary plots of mean currents in cells expressing shNT (n = 18 cells, 5 rats) versus shKCC2 (n = 21 cells, 7 rats). Bath application of bupivacaine (100 μM) reduced potassium currents only in control cells (shNT: n = 16 cells, 3 rats; shKCC2: n = 19 cells, 5 rats).

(I) Rectification index plot, defined as the ratio of potassium-mediated currents at −60 versus −120 mV.

(J) The difference in V_{rest} between control and KCC2-knockdown neurons is almost entirely suppressed by bath application of bupivacaine (100 μM). *$p < 0.05$; **$p < 0.01$; ***$p < 0.001$.

Immunofluorescence confocal imaging indeed revealed a reduced pericellular Task-3 expression in KCC2 knockdown as compared with control granule cells (Figure 3A). We then investigated the mechanisms underlying Task-3 downregulation upon KCC2 silencing. KCC2 has been shown to interact with a variety of proteins, including some that regulate KCC2 membrane expression (Ivakine et al., 2013; Mahadevan et al., 2017; Wright et al., 2017) or, conversely, are regulated through direct interaction with KCC2 (Chevy et al., 2015; Llano et al., 2015). We therefore asked whether KCC2 might also interact with Task-3 channels and thereby influence their membrane expression and/or function. Co-immunoprecipitation assays from adult rat hippocampal homogenates showed that anti-Task-3 antibodies pulled

down KCC2, indicating an interaction between the endogenous proteins in hippocampal neurons (Figure 3B). In order to characterize KCC2-Task-3 interaction further, we co-immunoprecipitated exogenously expressed FLAG-tagged KCC2 and human influenza hemagglutinin (HA)-tagged Task-3 in HEK293 cells. In lysates from double-transfected cells, anti-HA antibodies pulled down FLAG-KCC2 together with HA-Task-3, and anti-FLAG antibodies pulled down HA-Task-3 and FLAG-KCC2 (Figure 3C). However, overexpressed HA-tagged GFP failed to interact with KCC2 in a similar assay (Figure 3C). We then tested whether interaction with KCC2 may influence Task-3 channel expression. HA-Task-3 was expressed in Neuro-2A cells either alone or together with FLAG-KCC2, and HA-Task-3 expression was
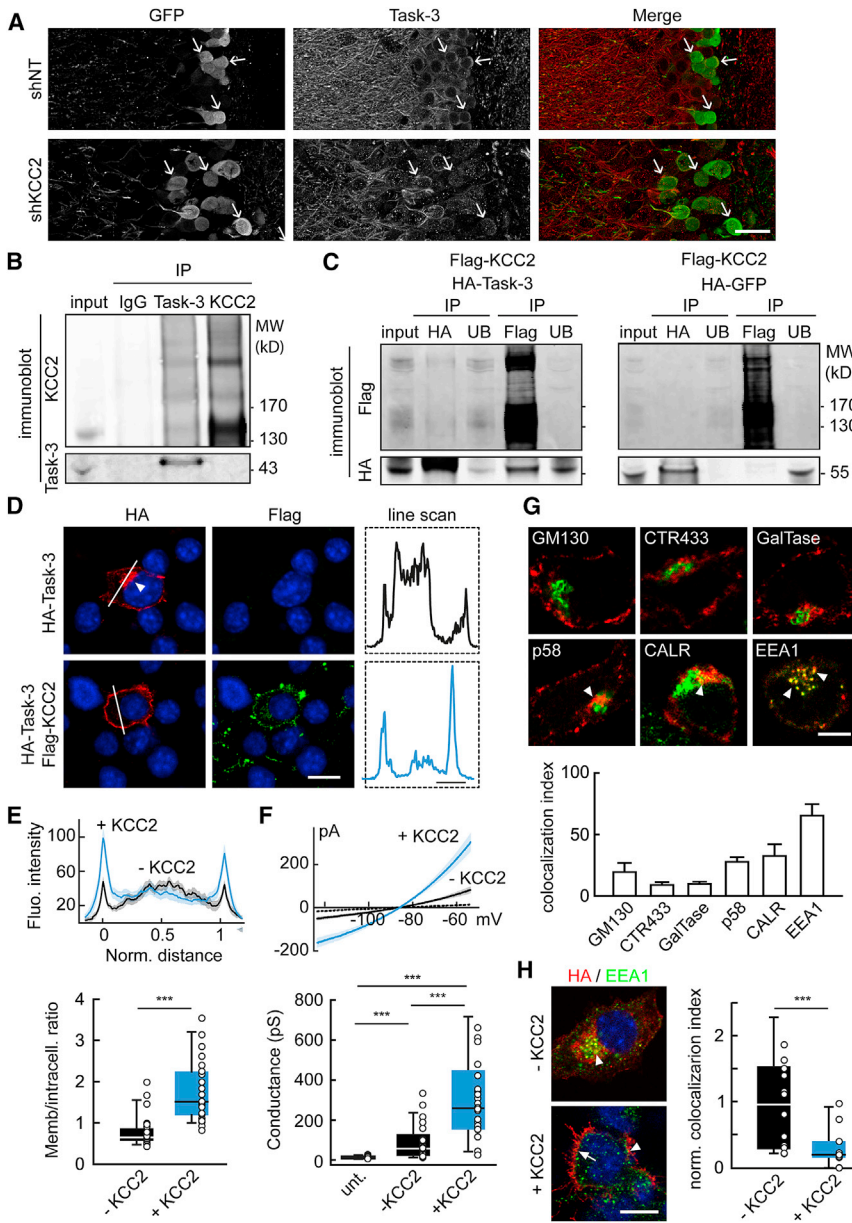
Figure 3. KCC2 Interacts with Task-3 and Promotes Its Membrane Expression

(A) Confocal micrographs of infected dentate gyrus, showing decreased Task-3 pericellular immunostaining in KCC2 knockdown versus control granule cells. Scale bar, 20 μm.

(B) Immunoblot of coIP samples from adult rat hippocampus extracts. Solubilized membrane homogenates (input) were immunoprecipitated with Task-3, KCC2, or control immunoglobulin G (IgG) antibodies. Eluates from immunoprecipitations (IP fractions) were then probed for both Task-3 and KCC2. Representative example of three independent replicates is shown.

(C) Immunoblot of the immunoprecipitates from HEK293 cell homogenates coexpressing FLAG-tagged KCC2 and HA-tagged Task-3 (left) or HA-tagged GFP (right). Immunoprecipitation using FLAG antibodies pulled down Task-3, but not GFP. Conversely, immunoprecipitation with HA antibodies precipitated FLAG-KCC2 only in HA-Task-3-expressing cells. Representative example of three independent experiments is shown.

(D) Representative confocal fluorescent micrographs of Neuro-2a cells transfected with either HA-Task-3 alone (top) or HA-Task-3 together with FLAG-KCC2 (bottom). Note intracellular accumulation of HA immunostaining in absence of FLAG-KCC2 (arrowhead). Scale bar, 10 μm. Fluorescence intensity of HA staining across the cell membrane and cytoplasm was analyzed along the white line shown on the micrographs and plotted in dotted insets (right). Scale bar, 5 μm.

(E) Averaged and scaled cross-section intensity plots from all cells (HA-Task-3, n = 24; HA-Task-3+FLAG-KCC2, n = 27; 3 independent experiments) reveal intracellular accumulation of Task-3 in absence of KCC2, as evidenced by the decreased ratio of pericellular to intracellular intensity (bottom).

(F) Averaged plots of leak potassium currents versus voltage recorded in Neuro-2a cells either untransfected (dotted line) or expressing mGFP together with HA-Task-3 alone (black line) or in combination with FLAG-KCC2 (blue line). n = 15, 25, and 25 cells, respectively, from 2 independent experiments.

(G) Top: representative confocal fluorescent micrographs of Neuro-2a cells expressing HA-Task-3 either alone or with the ERGIC marker p58-GFP

or the Golgi-resident recombinant enzyme GalTase-GFP. Cells were immunostained for HA (red) and markers of either *cis*-Golgi (GM130), medial Golgi (CTR433), endoplasmic reticulum (calregulin [CALR]), or early endosomes (EEA1, all in green). Arrowheads indicate colocalization of immunofluorescence between HA and the corresponding marker. Scale bar, 5 μm. Bottom: summary graph represents the colocalization index of HA immunofluorescence with each of the above markers (n = 5–20 cells for each marker; see STAR Methods).

(H) Left: representative confocal fluorescent micrographs of Neuro-2a cells expressing HA-Task-3 with or without FLAG-KCC2 and immunostained for HA (red), EEA1 (green), and DAPI (blue). Note the significant colocalization in cells lacking KCC2 (arrowheads), but not cells expressing KCC2, where HA immunofluorescence is mostly pericellular (arrow). Scale bar, 10 μm. Right: summary graph of HA and EEA1 colocalization in the absence (black) or presence (blue) of FLAG-KCC2. n = 15 and 11 cells, respectively, from 2 independent experiments. ***p < 0.001.

tested by immunostaining and confocal imaging. In the absence of KCC2, HA-Task-3 expression at plasma membrane was reduced and accumulated intracellularly (Figure 3D), with a reduced membrane to intracellular intensity ratio in cells lacking KCC2 (0.7 ± 0.1 versus 2.5 ± 0.3; Mann-Whitney; p = 1.6 × 10^{-7};

Figures 3D and 3E). Consistent with reduced Task-3 membrane expression, leak potassium conductance recorded from Neuro-2a cells transfected with HA-Task3 alone were significantly smaller than in cells co-expressing FLAG-KCC2 (87.0 ± 17.3 versus 319.8 ± 45.8 pS; Mann-Whitney; p = 2.4 × 10^{-5};

Figure 3F). Immunostaining or co-expression of sub-cellular compartment markers in Neuro-2A expressing HA-Task-3 alone revealed preferential accumulation of Task-3 proteins in early endosomes, as detected by colocalization of HA and early endosome antigen 1 (EEA1) immunofluorescence (Figure 3G). HA immunofluorescence also revealed some accumulation in the endoplasmic reticulum and the endoplasmic reticulum Golgi intermediate compartment (ERGIC), as identified by calregulin immunostaining and p58GFP expression, respectively, whereas very little colocalization was observed with markers of the Golgi complex GM130 (cis), CTR433 (median), and GalTase (Figure 3G). Finally, co-expression of HA-Task-3 together with KCC2 significantly reduced Task-3 colocalization with EEA1 by about 70% (Mann Whitney; $p = 3.6 \times 10^{-5}$; Figure 3H), suggesting KCC2 may influence Task-3 function at least in part through regulation of its membrane recycling.

We next asked how reduced leak conductance and enhanced excitability upon KCC2 suppression might affect EPSP/spike coupling in granule cells. Previous work showed that KCC2 knockdown in hippocampal neurons leads to reduced synaptic strength at glutamatergic inputs (Gauvain et al., 2011). Enhanced intrinsic excitability may then act as a homeostatic compensatory mechanism for reduced synaptic excitation. We tested this hypothesis by first comparing miniature excitatory postsynaptic currents (mEPSCs). As previously reported, KCC2 knockdown granule cells showed a ~20% decrease in mEPSC amplitude (5.1 ± 0.4 versus 6.5 ± 0.3 pA; Mann-Whitney; p = 0.0009; Figures 4A and 4B) with no significant change in their mean frequency (1.6 ± 0.4 versus 1.8 ± 0.4 Hz; Mann-Whitney; p = 0.09; Figures 4A and 4B) compared to control cells. From these recordings, waveforms of quantal currents were derived, fit, and used as a current command in current-clamp recordings from KCC2 knockdown versus control granule cells maintained at their resting membrane potential (Figure 4C). Although the efficacy of excitatory inputs was reduced in KCC2 knockdown neurons compared to control, enhanced intrinsic excitability overcompensated this reduction, leading to enhanced EPSP/spike coupling. Thus, KCC2 knockdown neurons fired action potentials from ~40 simultaneous quanta, whereas firing of control neurons required at least 60 quanta (Figure 4C; repeated-measures ANOVA; $F_{20,500} = 4.83$; p = 0.0374). In addition, synaptic integration during high-frequency (>50 Hz) trains of EPSCs was also facilitated in KCC2 knockdown granule cells, owing to increased membrane resistance compared to control cells (Figure 4D).

Perforant path input to the dentate gyrus provides synaptic excitation to granule cells as well as feedforward inhibition that contributes to their sparse activation by entorhinal afferents (Witter, 2007). We explored EPSP/spike coupling of perforant path inputs in a more physiological setting by recording evoked field EPSP (fEPSP) and population spike in a densely infected area of the granular layer, upon stimulation of perforant path inputs. In KCC2 knockdown slices, fEPSP/population spike coupling was increased by ~47% compared to control slices (2.0 ± 0.3 versus 1.3 ± 0.2 ms^{-1}; t test; $t_{29} = 2.18$; p = 0.0374; Figure 4F). This result further supports that increased excitability upon KCC2 knockdown is not homeostatic but instead acts to promote granule cell recruitment by entorhinal afferents.

Importantly, bath application of the GABAAR antagonist picrotoxin (100 μM) increased the amplitude of population spike similarly in control slices (1.1 ± 0.2 mV versus 0.9 ± 0.1 mV; paired t test; $t_{13} = 3.33$; p = 0.0054) and KCC2 knockdown slices (1.2 ± 0.2 mV versus 0.8 ± 0.1 mV; paired t test; $t_{15} = 4.29$; p = 0.0006; Figure 4G). These results suggest that GABAergic transmission, although depolarizing in dentate granule cells (Staley and Mody, 1992; Figure 1E), remains shunting and inhibitory, independent of KCC2 expression. Therefore, KCC2 downregulation in these cells promotes their recruitment by entorhinal afferents primarily through enhanced excitability and EPSP/spike coupling rather than altered GABA signaling.

The dentate gyrus is often considered as a filter or a gate for activity propagation from the entorhinal cortex to the hippocampus (Hsu, 2007), in particular owing to dentate granule cells' sparse firing. Enhanced EPSP/spike coupling in dentate granule cells upon KCC2 knockdown may then act to increase their excitatory drive by entorhinal afferents and thereby alter hippocampal rhythmogenesis. We explored this hypothesis using chronic intrahippocampal recordings from rats injected with lentivirus expressing either shKCC2 or shNT (n = 7 and 5, respectively; Figures 5A and 5B). In these animals, about 40%–70% granule cells were infected over 1 or 2 mm around the injection site (Figures 5B and S4A–S4C). Unlike a recent study using a similar approach (Chen et al., 2017), we did not observe spontaneous seizures in any of these animals. Susceptibility to pilocarpine-induced seizures was also unaffected by KCC2 knockdown in the dorsal dentate gyrus (Figures S4D–S4F). Chronic, intrahippocampal recordings using linear silicon probes did not reveal interictal spikes or fast ripples (Figures S4G and S4H) that could represent hallmarks of an epileptic hippocampal network, even in the absence of behavioral symptoms (Bragin et al., 1999). These results indicate that focal KCC2 knockdown in 40%–70% dorsal dentate granule cells is not sufficient to trigger or promote epileptiform activity.

Further analysis of hippocampal rhythmogenesis during various behavioral states, however, revealed significant alterations upon KCC2 knockdown in the dentate gyrus. Thus, although theta-band activity recorded during exploration and rapid-eye movement (REM) sleep was not significantly affected (Figure S5), we observed a specific increase in both the amplitude (Kolmogorov-Smirnov; p < 0.001; Figure 5F) and frequency (Kolmogorov-Smirnov; p < 0.001; Figure 5F) of dentate spikes during slow-wave sleep (SWS). Dentate spikes are sharp hilar local field potential (LFP) events associated with rest (Bragin et al., 1995) that arise from a transient increase in the excitatory drive from the entorhinal cortex, as revealed by current source density analysis (Figures 5D and 5E). Our results suggested these changes in dentate spike activity resulted primarily from increased excitability of dentate granule cells. Restoring granule cell excitability independently of chloride export and GABA signaling was then predicted to rescue dentate spike activity. We tested this prediction by co-injecting animals with adeno-associated viruses expressing the inhibitory receptor hM4D(Gi) (Roth, 2016) and either shNT or shKCC2. Using this approach, all granule cells expressing GFP also expressed hM4D(Gi), thereby enabling selective silencing of neurons expressing shRNA sequences (Figures 5G and 5H). We first verified that
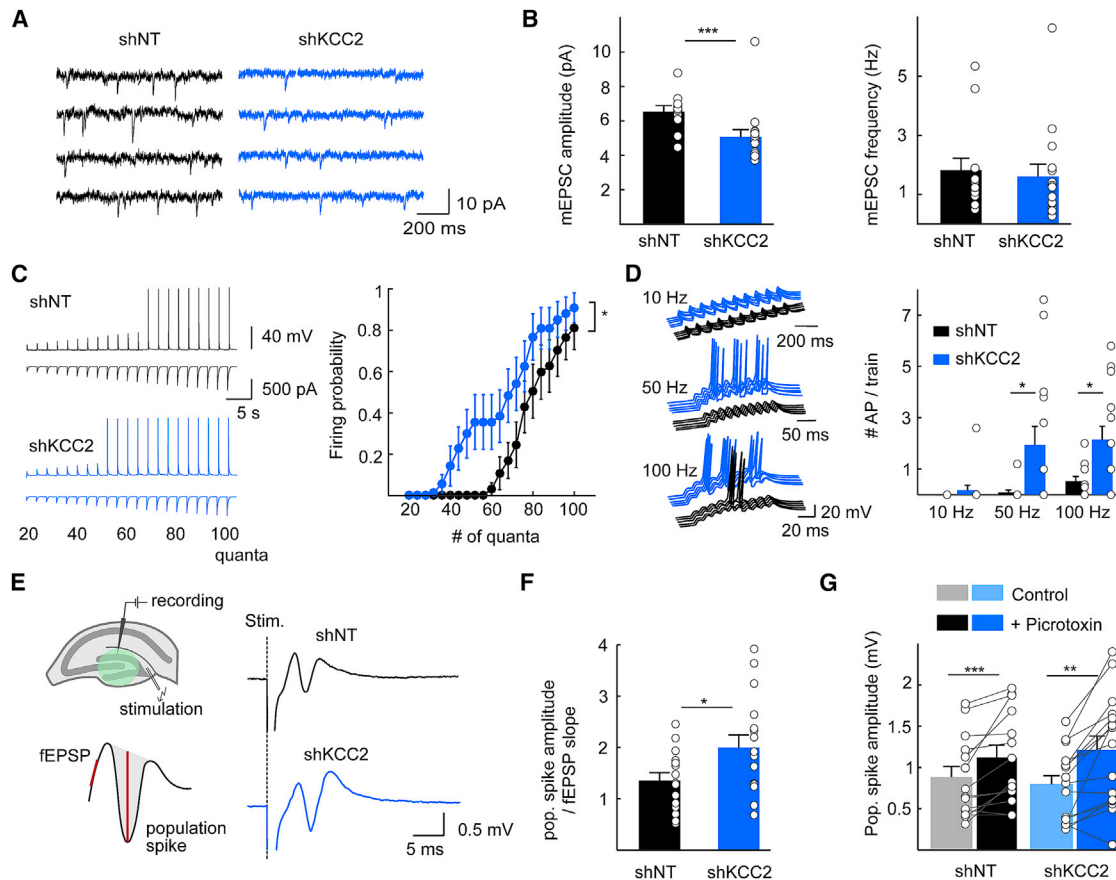
Figure 4. KCC2 Suppression Increases EPSP/Spike Coupling in Dentate Granule Cells

(A) 4-s recordings of mEPSCs from infected granule cells expressing shNT (black; n = 13 cells, 3 rats) or shKCC2 (blue; n = 15 cells, 3 rats).

(B) Summary data showing reduced mEPSC amplitude (left), but not frequency (right).

(C) Left: representative recordings of current clamp recordings (top) from granule cells kept at their resting membrane potential upon somatic injection of multiples of scaled, mEPSC waveforms of increasing amplitude (bottom). Right: summary plots of all data (shNT, n = 13 cells, 2 rats; shKCC2, n = 15 cells, 2 rats) show enhanced EPSP/spike coupling in KCC2 knockdown neurons.

(D) Neurons were kept at −87 mV in current clamp mode and trains of 120 pA mEPSCs (about 20× quantal size) were injected as in (C) at various frequencies. Left: representative traces for trains of 10 EPSC waveforms at 10, 50, and 100 Hz. Right: summary graphs show enhanced firing probability in KCC2 knockdown granule cells (shNT, n = 13 cells, 2 rats; shKCC2, n = 15 cells, 2 rats).

(E) Left: experimental paradigm to test synaptically evoked EPSP/spike coupling (top). fEPSP and population spike amplitudes were measured as shown (bottom). Right: average of 10 consecutive responses recorded at 0.1 Hz is shown.

(F) Data from n = 15 slices infected with shNT (6 animals) and 16 slices infected with shKCC2 (6 animals) confirmed increased coupling of fEPSP to population spike.

(G) Bath application of the GABAAR blocker picrotoxin resulted in increased amplitude of the population spike in both conditions, indicating GABA transmission was functionally inhibitory. *p < 0.05.

---

hM4D(Gi) activation was sufficient to hyperpolarize transduced granule cells *in vitro*. Indeed, in whole-cell recordings from transduced neurons, bath application of the hM4D(Gi) ligand CNO (10 μM) induced a hyperpolarizing shift of V_{rest} by −5.7 ± 1.4 mV (paired t test; $t_5 = 4.36$; p = 0.0073; Figure 5I). As in lentivirus-infected animals, adeno-associated virus (AAV)-mediated KCC2 knockdown in the dorsal dentate gyrus increased the amplitude and reduced the frequency of dentate spikes during SWS (n = 4 control and 3 KCC2 knockdown rats; Kolmogorov-Smirnov; p < 0.001; Figure 5J). Following systemic CNO injection, the amplitude of dentate spikes in animals injected with shKCC2 was reduced to levels below those of saline-treated control animals (Figure 5J). Similarly, CNO injection reduced the frequency of dentate spikes in both KCC2 knockdown and control animals (Kolmogorov-Smirnov; p < 0.001; Figure 5J). Together, our data demonstrate that KCC2 suppression in dentate granule cells leads to altered dentate gyrus activity through a reduced Task-3-mediated potassium conductance and a subsequent increase in neuronal excitability, independent of GABA signaling.

DISCUSSION

Cation-chloride cotransporters (CCCs) are essential to neuronal chloride homeostasis. Changes in their expression level in the
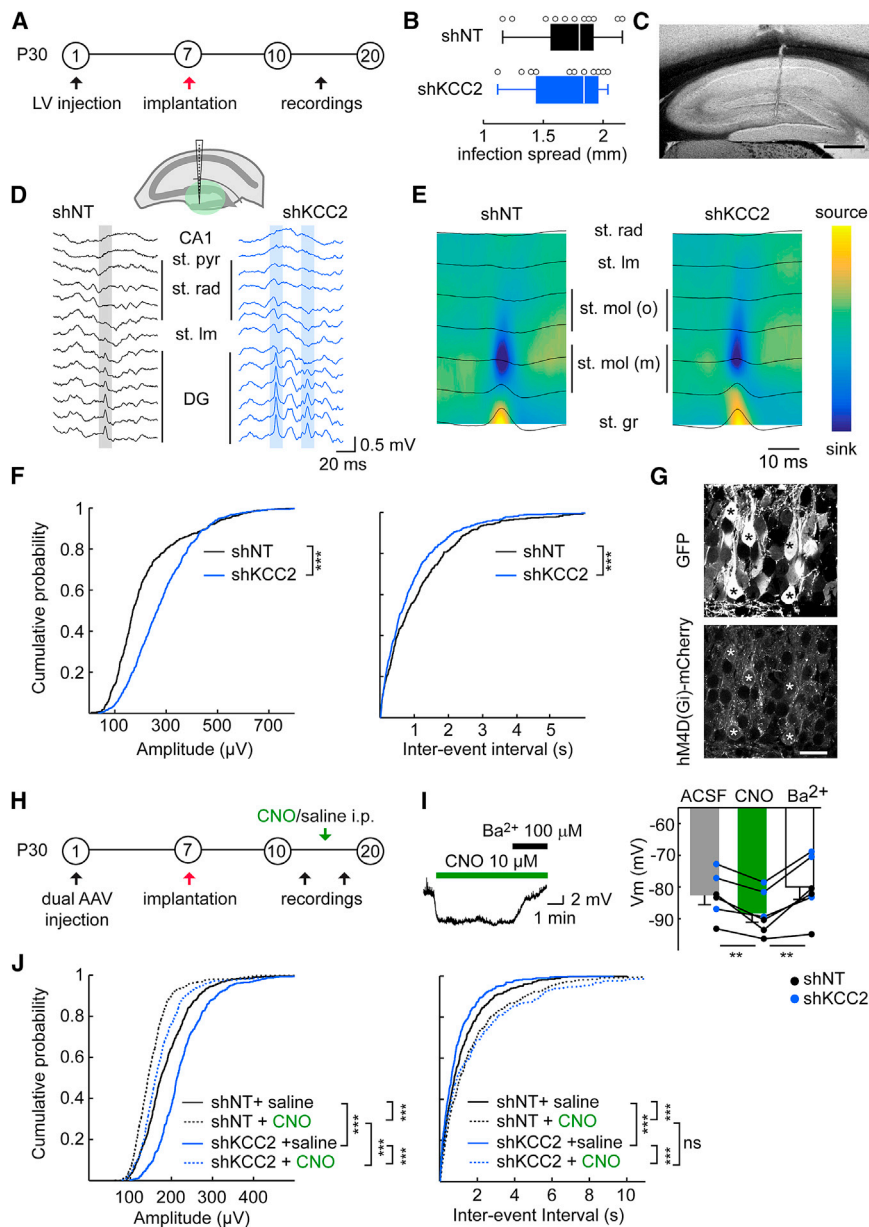
Figure 5. KCC2 Suppression Alters Dentate Gyrus Activity Primarily through Increased Neuronal Excitability

(A) Experimental timeline.

(B) Longitudinal spread of the viral infection determined at the end of each experiment (shNT: n = 5 rats; shKCC2: n = 7 rats; p = 0.45).

(C) Macroscope differential interference contrast (DIC) micrograph revealing probe localization (vertical scar). Scale bar, 250 μm.

(D) Top: representative recordings during non-REM sleep showing dentate spikes (highlighted in gray: shNT; blue: shKCC2).

(E) Averaged current source density plots of at least 100 events per animal reveal similar profiles between groups and allow identification of granule cell layer (presence of a source).

(F) Cumulative amplitude (left) and inter-event intervals (right) histograms of 140 randomly selected events per animal.

(G) Single plane confocal micrographs confirmed most granule cells were co-infected with shRNA[+]GFP and hM4D(Gi)-mCherry (stars). Scale bar, 20 μm.

(H) Experimental timeline for rescue experiments with DREADD silencing as above.

(I) Left: example current clamp recording of a dentate granule cell expressing shNT and hM4D(Gi) receptor, showing hyperpolarization of the membrane potential upon CNO (10 μM) bath application. Application of Ba^{2+} (100 mM $BaCl_2$) completely blocks CNO-induced hyperpolarization. Right: summary data from 3 cells expressing shNT and 3 cells expressing shKCC2 together with hM4D(Gi). All cells were hyperpolarized following CNO application and repolarized upon Ba^{2+} application. **p < 0.01.

(J) Cumulative amplitude (left) and inter-event intervals (right) histograms from 185 randomly selected events per animal (shNT n = 4 rats; shKCC2 n = 3 rats). ***p < 0.001.

dentate granule cells has little effect on GABA signaling at rest but instead increases their excitability due to reduced expression of Task-3 potassium channels. This increased excitability strengthens EPSP/spike coupling in granule cells, thereby acting to enhance their recruitment by entorhinal afferents. This in turn results in altered local rhythmogenesis that was normalized by restoring granule cell intrinsic excitability. Thus, KCC2 downregulation affects a variety of synaptic and intrinsic properties in hippocampal neurons beyond the mere control of GABA transmission and concurs to perturb hippocampal activity.

KCC2 interacts with a variety of transmembrane as well as intracellular partners, including postsynaptic receptors (Mahadevan et al., 2014; Wright et al., 2017; Ivakine et al., 2013), actin-related proteins (Chevy et al., 2015; Li et al., 2007; Llano et al., 2015), and others involved in protein trafficking and recycling (Mahadevan et al., 2017). Although these interactions are

developing brain are associated with changes in the polarity of GABA transmission (Rivera et al., 1999), and altered CCC function or expression is observed in a variety of neurological and psychiatric conditions (Kahle et al., 2008; Kaila et al., 2014). In the pathology, KCC2 downregulation is often assumed to primarily affect GABA signaling and thereby promote hyperexcitability (Ben-Ari, 2017; Boulenguez et al., 2010; Buchin et al., 2016; Dargaei et al., 2018; Gagnon et al., 2013; Huberfeld et al., 2007). However, this hypothesis was not tested in isolation from other, potentially confounding pathological factors. Here, we directly tested the impact of a chronic KCC2 knockdown on the cellular and synaptic properties of hippocampal neurons as well as on network activity associated with behavior. We demonstrate KCC2 knockdown in

most often considered with regard to KCC2 expression or function, they also influence the function of KCC2 partners (Chevy et al., 2015; Llano et al., 2015). Here, we identified the leak potassium channel Task-3 (KCNK9) as a KCC2 interactor in hippocampal neurons. We show Task-3 membrane expression and function requires KCC2 co-expression both in neurons and in heterologous cells. Immunocytochemical analysis revealed predominant accumulation of Task-3 proteins in early endosomes and, to a lesser extent, endoplasmic reticulum (ER) and ERGICs. This suggests that, at least in heterologous cells overexpressing recombinant Task-3, membrane expression of the protein is limited by endocytosis and/or ER sequestration. Regulation of Task-3 channel expression through endocytosis was recently reported upon stress-kinase activation (Cornell and Toyo-Oka, 2017). Whether KCC2 co-expression also reduced ER retention was not specifically examined here. However, it is remarkable that several members of the *YWHA* family encoding 14-3-3 proteins were recently identified as putative KCC2 partners (Mahadevan et al., 2017). 14-3-3 are adaptor proteins shown to bind to and influence the membrane traffic in particular of both Task-1 and Task-3 channels (Zuzarte et al., 2009). Thus, phosphorylation-dependent binding of 14-3-3 suppresses coatomer protein I (COPI)-mediated ER retention of Task channels (Kilisch et al., 2016; Zuzarte et al., 2009). KCC2 binding to both 14-3-3 and Task-3 may therefore influence their interaction, thereby preventing COPI-mediated intracellular sequestration of the channels.

Hippocampal granule cells express several leak potassium channels (Aller and Wisden, 2008), including Twik-1 and 2 (KCNK1 and KCNK6), Task-3 (KCNK9; Zhang et al., 2016), and Trek-2 (KCNK10). Our pharmacological and biophysical data (Figures 2G–2J) suggest KCC2 knockdown mostly affects bupivacaine-sensitive, outwardly rectifying channels, therefore limiting the potential targets to Task-3 and Trek-2 channels. We show Trek-2 are expressed mostly in mossy fibers and are therefore unlikely to significantly contribute to granule cell membrane resistance. Therefore, we mostly explored the impact of KCC2 knockdown on Task-3 channel expression and function. Nevertheless, it should be noted that K2P channels can form functional heterodimers (Levitz et al., 2016), and we cannot exclude that KCC2 may be part of a macromolecular complex involving other K2P channel subtypes. Finally, K2P channels are sensitive to both intracellular and extracellular pH (Noël et al., 2011). Because chloride gradients are used to control intracellular pH and KCC2 can effectively transport ammonium ions (Titz et al., 2006), it could be expected that K2P function may be affected upon KCC2 knockdown due to changes in either intracellular or extracellular pH. This, however, seems unlikely to contribute to the reduced leak potassium currents we observed as (1) our whole-cell recordings were performed with HEPES-buffered intracellular solution (Figure 2), (2) this effect was not observed in neighboring uninfected granule cells, and (3) prolonged application of the KCC2 antagonist VU0463271 had no effect on granule cell membrane potential or membrane resistance (Figure S1).

In mature neurons, KCC2 plays a prominent role in maintaining transmembrane chloride gradients, thereby influencing ion flux through the chloride-permeable GABAA receptor channels.

Thus, KCC2 pharmacological blockade (Ivakine et al., 2013; Wright et al., 2017), genetic ablation (Seja et al., 2012; Hübner et al., 2001), knockdown (Pellegrino et al., 2011), or activity-dependent modulation (Wright et al., 2017; Fiumelli et al., 2005; Heubl et al., 2017; Lee et al., 2010) all result in a depolarization of the reversal potential of GABAAR-mediated currents (E_{GABA}). Consistent with these observations, we found that chronic KCC2 knockdown in dentate granule cells resulted in a depolarizing shift of E_{GABA} by about 9 mV. This effect was, however, almost fully compensated by a depolarization of their resting membrane potential (V_{rest}) of about the same magnitude (Figure 1), resulting in a driving force of GABAAR currents that was virtually unaffected at rest. This effect was not specific of dentate gyrus granule cells, as it was observed also in CA1 pyramidal neurons (Figure S2). Despite the importance of the membrane potential in setting the efficacy and polarity of GABA signaling, only one study investigated the effect of KCC2 suppression on V_{rest} in cerebellar neurons (Seja et al., 2012). Thus, conditional KCC2 ablation resulted in a depolarization of V_{rest} that also compensated the shift in E_{GABA} in granule cells, but not Purkinje cells. Interestingly, hippocampal and cerebellar granule cells as well as CA1 pyramidal cells strongly express Task-3 channels (Marinc et al., 2014; Ramadoss et al., 2008), whereas Purkinje cells predominantly express Task-1 and Task-5 (Ramadoss et al., 2008; Karschin et al., 2001). Thus, differential expression of leak potassium channels may underlie cell-specific effects of KCC2 knockdown on resting membrane potential and the driving force of GABAAR currents.

KCC2 downregulation has often been linked to epileptogenesis. KCC2 expression is reduced in several animal models of experimental epilepsy, including kindling (Rivera et al., 2004), traumatic brain injury (Bonislawski et al., 2007), and pilocarpine-induced *status epilepticus* (Kourdougli et al., 2017). Moreover, genetic studies identified loss-of-function mutations in the SLC12A5 gene encoding KCC2 in families with idiopathic epilepsy (Kahle et al., 2014; Merner et al., 2015; Saitsu et al., 2016). Finally, lack of KCC2 expression was associated with depolarized E_{GABA} in 20%–30% principal neurons in the subiculum resected from temporal lobe epilepsy patients (Huberfeld et al., 2007), as well as in human peritumoral neocortical slices (Pallud et al., 2014). This work suggested that KCC2 downregulation may be causal to the pathological, interictal activity recorded *in vitro*, and a modeling study supported such conclusion (Buchin et al., 2016). Our experiments allowed us to test this hypothesis. Despite a high density and widespread infection in most of the dorsal dentate gyrus, we did not, however, find any sign of epileptiform activity in rats with suppressed KCC2 expression (Figure S4). Thus, these animals did not show spontaneous seizures, and intrahippocampal recordings around the infected area failed to reveal interictal discharges or fast ripples that occur between seizures both in patients and in animal models of focal epilepsy (Lévesque et al., 2018; Menendez de la Prida and Trevelyan, 2011). Susceptibility to pilocarpine-evoked *status epilepticus* was also unaffected by KCC2 knockdown. Our data therefore argue against a causal link between KCC2 downregulation and the emergence of epileptiform activity, at least in the dentate gyrus. Several arguments may help resolve this apparent discrepancy between our results and

data from human epileptic tissue and animal models. First, epileptic networks undergo a number of physio-pathological alterations that may contribute to or promote epileptiform activities, including cell death, axonal sprouting, inflammation, as well as changes in synaptic and intrinsic neuronal membrane properties (Goldberg and Coulter, 2013). Thus, it is interesting to note that KCC2 suppression failed to produce epileptiform activity in a subicular model network unless extracellular potassium was raised to a non-physiological range, thereby increasing neuronal excitability (Buchin et al., 2016). In addition, our data show that depolarized E_{GABA} upon KCC2 suppression is fully compensated by depolarized V_{rest}, such that KCC2 knockdown neurons are more excitable, although GABA signaling remains inhibitory. Depolarizing GABAergic responses may then require further depolarization of E_{GABA}, for instance through concomitant upregulation of the NKCC1 transporter, as observed in temporal lobe epilepsy models (Kourdougli et al., 2017; Wang et al., 2017) as well as in the cortex and hippocampus from epileptic patients (Pallud et al., 2014; Sen et al., 2007).

Our results show that KCC2 downregulation in the dentate gyrus is nevertheless sufficient to alter local rhythmogenesis. Thus, we report a specific increase in the amplitude and frequency of dentate spikes upon KCC2 knockdown (Figure 5). Dentate spikes are population activities that occur in the dentate gyrus during sleep and immobility and are thought to represent synchronous activation of granule cells by entorhinal afferents (Bragin et al., 1995). Although granule cells fire sparsely under physiological conditions, KCC2 suppression and subsequent increased excitability promoted their recruitment by entorhinal afferents. Thus, fewer simultaneous quantal EPSCs were required for firing KCC2 knockdown granule cells, and they fired more action potentials than control cells during high-frequency trains of afferent inputs (Figures 4C and 4D). Several arguments support that these effects were mostly independent of KCC2-induced alterations in GABA transmission. First, GABA transmission was still inhibitory upon KCC2 suppression, as indicated by the unchanged driving force of GABAAR-mediated currents (Figure 1) and the excitatory effect of picrotoxin on evoked population spikes (Figure 4G). Second, increased dentate spike amplitude was fully compensated by chemogenetic hyperpolarization of KCC2 knockdown neurons (Figure 5). Because GABAAR activation is depolarizing in dentate granule cells (Staley and Mody, 1992), hM4D(Gi)-induced hyperpolarization rescued V_{rest} in infected granule cells but further enhanced the depolarizing nature of GABA transmission. If GABA signaling was involved in the increased dentate spike amplitude and frequency, hM4D(Gi) silencing would then be expected to worsen, not rescue this phenotype.

Together, our work reveals the unexpected effects of a chronic downregulation of KCC2 expression in an intact network. We show these effects are diverse but primarily involve increased neuronal excitability, not reversed GABA signaling. They lead to altered network activity without, however, promoting seizures. Thus, KCC2 suppression in the dentate gyrus primarily affects dentate spike activity with no detectable effect on theta-band activity throughout the hippocampal formation (Figure S5). This rather subtle phenotype may still be of physiopathological relevance for disorders associated with KCC2 downregulation.

Dentate spikes coincide with periods of stronger gamma-band activity coherence between hippocampus and cortex and are temporally correlated to the power of sharp-wave ripples (Headley et al., 2017). Because both dentate spikes (Nokia et al., 2017) and sharp-wave ripples (Girardeau et al., 2009) have been associated with memory consolidation in hippocampal-dependent learning, we predict KCC2 suppression in the pathology may impact cognitive performances through a combination of GABA-dependent and independent mechanisms. Our results suggest therapeutic strategies aiming to either restore neuronal chloride homeostasis by blocking NKCC1 function (Ben-Ari, 2017) and neuronal excitability by targeting leak potassium channels (Loucif et al., 2018) or to stabilize KCC2 membrane expression (Gagnon et al., 2013; Liabeuf et al., 2017) may best compensate for altered network activity and associated behavioral or cognitive deficits.

STAR★METHODS

Detailed methods are provided in the online version of this paper and include the following:

- KEY RESOURCES TABLE
- LEAD CONTACT AND MATERIALS AVAILABILITY
- EXPERIMENTAL MODEL AND SUBJECT DETAILS
  - Animals
  - HEK293 and Neuro-2a cultures
  - Primary hippocampal cultures
- METHOD DETAILS
  - Virus and constructs
  - Stereotaxic viral injection and EcoG electrode implantation
  - Intracerebral probe implantation
  - Electrophysiology
  - Biochemistry
  - Immunocytochemistry
  - Immunohistochemistry
  - Behavior and recordings
  - Data analysis
  - Electrocorticogram (EcoG) recordings and epilepsy induction
- QUANTIFICATION AND STATISTICAL ANALYSIS
  - Statistics

SUPPLEMENTAL INFORMATION

Supplemental Information can be found online at https://doi.org/10.1016/j.celrep.2019.06.001.

AUTHOR CONTRIBUTIONS

DECLARATION OF INTERESTS

REFERENCES

Aller, M.I., and Wisden, W. (2008). Changes in expression of some two-pore domain potassium channel genes (KCNK) in selected brain regions of developing mice. Neuroscience *151*, 1154–1172.

Ankri, N., Legendre, P., Faber, D.S., and Korn, H. (1994). Automatic detection of spontaneous synaptic responses in central neurons. J. Neurosci. Methods *52*, 87–100.

Banerjee, A., Rikhye, R.V., Breton-Provencher, V., Tang, X., Li, C., Li, K., Runyan, C.A., Fu, Z., Jaenisch, R., and Sur, M. (2016). Jointly reduced inhibition and excitation underlies circuit-wide changes in cortical processing in Rett syndrome. Proc. Natl. Acad. Sci. USA *113*, E7287–E7296.

Ben-Ari, Y. (2017). NKCC1 Chloride Importer Antagonists Attenuate Many Neurological and Psychiatric Disorders. Trends Neurosci. *40*, 536–554.

Blaesse, P., Airaksinen, M.S., Rivera, C., and Kaila, K. (2009). Cation-chloride cotransporters and neuronal function. Neuron *61*, 820–838.

Bonislawski, D.P., Schwarzbach, E.P., and Cohen, A.S. (2007). Brain injury impairs dentate gyrus inhibitory efficacy. Neurobiol. Dis. *25*, 163–169.

Bormann, J., Hamill, O.P., and Sakmann, B. (1987). Mechanism of anion permeation through channels gated by glycine and gamma-aminobutyric acid in mouse cultured spinal neurones. J. Physiol. *385*, 243–286.

Boulenguez, P., Liabeuf, S., Bos, R., Bras, H., Jean-Xavier, C., Brocard, C., Stil, A., Darbon, P., Cattaert, D., Delpire, E., et al. (2010). Down-regulation of the potassium-chloride cotransporter KCC2 contributes to spasticity after spinal cord injury. Nat. Med. *16*, 302–307.

Bragin, A., Jandó, G., Nádasdy, Z., van Landeghem, M., and Buzsáki, G. (1995). Dentate EEG spikes and associated interneuronal population bursts in the hippocampal hilar region of the rat. J. Neurophysiol. *73*, 1691–1705.

Bragin, A., Engel, J., Jr., Wilson, C.L., Vizentin, E., and Mathern, G.W. (1999). Electrophysiologic analysis of a chronic seizure model after unilateral hippocampal KA injection. Epilepsia *40*, 1210–1221.

Buchin, A., Chizhov, A., Huberfeld, G., Miles, R., and Gutkin, B.S. (2016). Reduced Efficacy of the KCC2 Cotransporter Promotes Epileptic Oscillations in a Subiculum Network Model. J. Neurosci. *36*, 11619–11633.

Caraiscos, V.B., Elliott, E.M., You-Ten, K.E., Cheng, V.Y., Belelli, D., Newell, J.G., Jackson, M.F., Lambert, J.J., Rosahl, T.W., Wafford, K.A., et al. (2004). Tonic inhibition in mouse hippocampal CA1 pyramidal neurons is mediated by alpha5 subunit-containing gamma-aminobutyric acid type A receptors. Proc. Natl. Acad. Sci. USA *101*, 3662–3667.

Chamma, I., Heubl, M., Chevy, Q., Renner, M., Moutkine, I., Eugène, E., Poncer, J.C., and Lévi, S. (2013). Activity-dependent regulation of the K/Cl transporter KCC2 membrane diffusion, clustering, and function in hippocampal neurons. J. Neurosci. *33*, 15488–15503.

Chen, L., Wan, L., Wu, Z., Ren, W., Huang, Y., Qian, B., and Wang, Y. (2017). KCC2 downregulation facilitates epileptic seizures. Sci. Rep. *7*, 156.

Chevy, Q., Heubl, M., Goutierre, M., Backer, S., Moutkine, I., Eugène, E., Bloch-Gallego, E., Lévi, S., and Poncer, J.C. (2015). KCC2 Gates Activity-Driven AMPA Receptor Traffic through Cofilin Phosphorylation. J. Neurosci. *35*, 15772–15786.

Côme, E., Heubl, M., Schwartz, E.J., Poncer, J.C., and Lévi, S. (2019). Reciprocal Regulation of KCC2 Trafficking and Synaptic Activity. Front. Cell. Neurosci. *13*, 48.

Cornell, B., and Toyo-Oka, K. (2017). 14-3-3 Proteins in Brain Development: Neurogenesis, Neuronal Migration and Neuromorphogenesis. Front. Mol. Neurosci. *10*, 318.

Coull, J.A., Boudreau, D., Bachand, K., Prescott, S.A., Nault, F., Sík, A., De Koninck, P., and De Koninck, Y. (2003). Trans-synaptic shift in anion gradient in spinal lamina I neurons as a mechanism of neuropathic pain. Nature *424*, 938–942.

Dargaei, Z., Bang, J.Y., Mahadevan, V., Khademullah, C.S., Bedard, S., Parfitt, G.M., Kim, J.C., and Woodin, M.A. (2018). Restoring GABAergic inhibition rescues memory deficits in a Huntington's disease mouse model. Proc. Natl. Acad. Sci. USA *115*, E1618–E1626.

Deidda, G., Parrini, M., Naskar, S., Bozarth, I.F., Contestabile, A., and Cancedda, L. (2015). Reversing excitatory GABAAR signaling restores synaptic plasticity and memory in a mouse model of Down syndrome. Nat. Med. *21*, 318–326.

Delpire, E., Baranczak, A., Waterson, A.G., Kim, K., Kett, N., Morrison, R.D., Daniels, J.S., Weaver, C.D., and Lindsley, C.W. (2012). Further optimization of the K-Cl cotransporter KCC2 antagonist ML077: development of a highly selective and more potent in vitro probe. Bioorg. Med. Chem. Lett. *22*, 4532–4535.

Di Cristo, G., Awad, P.N., Hamidi, S., and Avoli, M. (2018). KCC2, epileptiform synchronization, and epileptic disorders. Prog. Neurobiol. *162*, 1–16.

Fiumelli, H., Cancedda, L., and Poo, M.M. (2005). Modulation of GABAergic transmission by activity via postsynaptic Ca2+-dependent regulation of KCC2 function. Neuron *48*, 773–786.

Gagnon, M., Bergeron, M.J., Lavertu, G., Castonguay, A., Tripathy, S., Bonin, R.P., Perez-Sanchez, J., Boudreau, D., Wang, B., Dumas, L., et al. (2013). Chloride extrusion enhancers as novel therapeutics for neurological diseases. Nat. Med. *19*, 1524–1528.

Gauvain, G., Chamma, I., Chevy, Q., Cabezas, C., Irinopoulou, T., Bodrug, N., Carnaud, M., Lévi, S., and Poncer, J.C. (2011). The neuronal K-Cl cotransporter KCC2 influences postsynaptic AMPA receptor content and lateral diffusion in dendritic spines. Proc. Natl. Acad. Sci. USA *108*, 15474–15479.

Girardeau, G., Benchenane, K., Wiener, S.I., Buzsáki, G., and Zugaro, M.B. (2009). Selective suppression of hippocampal ripples impairs spatial memory. Nat. Neurosci. *12*, 1222–1223.

Goldberg, E.M., and Coulter, D.A. (2013). Mechanisms of epileptogenesis: a convergence on neural circuit dysfunction. Nat. Rev. Neurosci. *14*, 337–349.

Headley, D.B., Kanta, V., and Paré, D. (2017). Intra- and interregional cortical interactions related to sharp-wave ripples and dentate spikes. J. Neurophysiol. *117*, 556–565.

Heubl, M., Zhang, J., Pressey, J.C., Al Awabdh, S., Renner, M., Gomez-Castro, F., Moutkine, I., Eugène, E., Russeau, M., Kahle, K.T., et al. (2017). GABAA receptor dependent synaptic inhibition rapidly tunes KCC2 activity via the Cl⁻-sensitive WNK1 kinase. Nat. Commun. *8*, 1776.

Hsu, D. (2007). The dentate gyrus as a filter or gate: a look back and a look ahead. Prog. Brain Res. *163*, 601–613.

Huberfeld, G., Wittner, L., Clemenceau, S., Baulac, M., Kaila, K., Miles, R., and Rivera, C. (2007). Perturbed chloride homeostasis and GABAergic signaling in human temporal lobe epilepsy. J. Neurosci. *27*, 9866–9873.

Hübner, C.A., Stein, V., Hermans-Borgmeyer, I., Meyer, T., Ballanyi, K., and Jentsch, T.J. (2001). Disruption of KCC2 reveals an essential role of K-Cl cotransport already in early synaptic inhibition. Neuron *30*, 515–524.

Hyde, T.M., Lipska, B.K., Ali, T., Mathew, S.V., Law, A.J., Metitiri, O.E., Straub, R.E., Ye, T., Colantuoni, C., Herman, M.M., et al. (2011). Expression of GABA signaling molecules KCC2, NKCC1, and GAD1 in cortical development and schizophrenia. J. Neurosci. *31*, 11088–11095.

Ivakine, E.A., Acton, B.A., Mahadevan, V., Ormond, J., Tang, M., Pressey, J.C., Huang, M.Y., Ng, D., Delpire, E., Salter, M.W., et al. (2013). Neto2 is a KCC2 interacting protein required for neuronal Cl- regulation in hippocampal neurons. Proc. Natl. Acad. Sci. USA *110*, 3561–3566.

Jasmin, B.J., Cartaud, J., Bornens, M., and Changeux, J.P. (1989). Golgi apparatus in chick skeletal muscle: changes in its distribution during end plate development and after denervation. Proc. Natl. Acad. Sci. USA *86*, 7218–7222.

Kahle, K.T., Staley, K.J., Nahed, B.V., Gamba, G., Hebert, S.C., Lifton, R.P., and Mount, D.B. (2008). Roles of the cation-chloride cotransporters in neurological disease. Nat. Clin. Pract. Neurol. *4*, 490–503.

Kahle, K.T., Merner, N.D., Friedel, P., Silayeva, L., Liang, B., Khanna, A., Shang, Y., Lachance-Touchette, P., Bourassa, C., Levert, A., et al. (2014). Genetically encoded impairment of neuronal KCC2 cotransporter function in human idiopathic generalized epilepsy. EMBO Rep. *15*, 766–774.

Kahle, K.T., Schmouth, J.F., Lavastre, V., Latremoliere, A., Zhang, J., Andrews, N., Omura, T., Laganière, J., Rochefort, D., Hince, P., et al. (2016). Inhibition of the kinase WNK1/HSN2 ameliorates neuropathic pain by restoring GABA inhibition. Sci. Signal. *9*, ra32.

Kaila, K., Price, T.J., Payne, J.A., Puskarjov, M., and Voipio, J. (2014). Cation-chloride cotransporters in neuronal development, plasticity and disease. Nat. Rev. Neurosci. *15*, 637–654.

Karschin, C., Wischmeyer, E., Preisig-Müller, R., Rajan, S., Derst, C., Grzeschik, K.H., Daut, J., and Karschin, A. (2001). Expression pattern in brain of TASK-1, TASK-3, and a tandem pore domain K(+) channel subunit, TASK-5, associated with the central auditory nervous system. Mol. Cell. Neurosci. *18*, 632–648.

Ketchum, K.A., Joiner, W.J., Sellers, A.J., Kaczmarek, L.K., and Goldstein, S.A. (1995). A new family of outwardly rectifying potassium channel proteins with two pore domains in tandem. Nature *376*, 690–695.

Kilisch, M., Lytovchenko, O., Arakel, E.C., Bertinetti, D., and Schwappach, B. (2016). A dual phosphorylation switch controls 14-3-3-dependent cell surface expression of TASK-1. J. Cell Sci. *129*, 831–842.

Kourdougli, N., Pellegrino, C., Renko, J.M., Khirug, S., Chazal, G., Kukko-Lukjanov, T.K., Lauri, S.E., Gaiarsa, J.L., Zhou, L., Peret, A., et al. (2017). Depolarizing GABA contributes to glutamatergic network rewiring in epilepsy. Ann. Neurol. *81*, 251–265.

Lee, H.H., Jurd, R., and Moss, S.J. (2010). Tyrosine phosphorylation regulates the membrane trafficking of the potassium chloride co-transporter KCC2. Mol. Cell. Neurosci. *45*, 173–179.

Lee, H.H., Deeb, T.Z., Walker, J.A., Davies, P.A., and Moss, S.J. (2011). NMDA receptor activity downregulates KCC2 resulting in depolarizing GABAA receptor-mediated currents. Nat. Neurosci. *14*, 736–743.

Lesage, F., and Lazdunski, M. (2000). Molecular and functional properties of two-pore-domain potassium channels. Am. J. Physiol. Renal Physiol. *279*, F793–F801.

Lévesque, M., Salami, P., Shiri, Z., and Avoli, M. (2018). Interictal oscillations and focal epileptic disorders. Eur. J. Neurosci. *48*, 2915–2927.

Levitz, J., Royal, P., Comoglio, Y., Wdziekonski, B., Schaub, S., Clemens, D.M., Isacoff, E.Y., and Sandoz, G. (2016). Heterodimerization within the TREK channel subfamily produces a diverse family of highly regulated potassium channels. Proc. Natl. Acad. Sci. USA *113*, 4194–4199.

Li, H., Khirug, S., Cai, C., Ludwig, A., Blaesse, P., Kolikova, J., Afzalov, R., Coleman, S.K., Lauri, S., Airaksinen, M.S., et al. (2007). KCC2 interacts with the dendritic cytoskeleton to promote spine development. Neuron *56*, 1019–1033.

Liabeuf, S., Stuhl-Gourmand, L., Gackière, F., Mancuso, R., Sanchez Brualla, I., Marino, P., Brocard, F., and Vinay, L. (2017). Prochlorperazine Increases KCC2 Function and Reduces Spasticity after Spinal Cord Injury. J. Neurotrauma *34*, 3397–3406.

Llano, O., Smirnov, S., Soni, S., Golubtsov, A., Guillemin, I., Hotulainen, P., Medina, I., Nothwang, H.G., Rivera, C., and Ludwig, A. (2015). KCC2 regulates actin dynamics in dendritic spines via interaction with β-PIX. J. Cell Biol. *209*, 671–686.

Loucif, A.J.C., Saintot, P.P., Liu, J., Antonio, B.M., Zellmer, S.G., Yoger, K., Veale, E.L., Wilbrey, A., Omoto, K., Cao, L., Gutteridge, A., Castle, N.A., Stevens, E.B., and Mathie, A. (2018). GI-530159, a novel, selective, mechanosensitive two-pore-domain potassium (K2P) channel opener, reduces rat dorsal root ganglion neuron excitability. Br. J. Pharmacol. *175*, 2272–2283.

Mahadevan, V., and Woodin, M.A. (2016). Regulation of neuronal chloride homeostasis by neuromodulators. J. Physiol. *594*, 2593–2605.

Mahadevan, V., Pressey, J.C., Acton, B.A., Uvarov, P., Huang, M.Y., Chevrier, J., Puchalski, A., Li, C.M., Ivakine, E.A., Airaksinen, M.S., et al. (2014). Kainate receptors coexist in a functional complex with KCC2 and regulate chloride homeostasis in hippocampal neurons. Cell Rep. *7*, 1762–1770.

Mahadevan, V., Khademullah, C.S., Dargaei, Z., Chevrier, J., Uvarov, P., Kwan, J., Bagshaw, R.D., Pawson, T., Emili, A., De Koninck, Y., et al. (2017). Native KCC2 interactome reveals PACSIN1 as a critical regulator of synaptic inhibition. eLife *6*, e28270.

Marinc, C., Derst, C., Prüss, H., and Veh, R.W. (2014). Immunocytochemical localization of TASK-3 protein (K2P9.1) in the rat brain. Cell. Mol. Neurobiol. *34*, 61–70.

Medina, I., Friedel, P., Rivera, C., Kahle, K.T., Kourdougli, N., Uvarov, P., and Pellegrino, C. (2014). Current view on the functional regulation of the neuronal K(+)-Cl(-) cotransporter KCC2. Front. Cell. Neurosci. *8*, 27.

Menendez de la Prida, L., and Trevelyan, A.J. (2011). Cellular mechanisms of high frequency oscillations in epilepsy: on the diverse sources of pathological activities. Epilepsy Res. *97*, 308–317.

Merner, N.D., Chandler, M.R., Bourassa, C., Liang, B., Khanna, A.R., Dion, P., Rouleau, G.A., and Kahle, K.T. (2015). Regulatory domain or CpG site variation in SLC12A5, encoding the chloride transporter KCC2, in human autism and schizophrenia. Front. Cell. Neurosci. *9*, 386.

Noël, J., Sandoz, G., and Lesage, F. (2011). Molecular regulations governing TREK and TRAAK channel functions. Channels (Austin) *5*, 402–409.

Nokia, M.S., Gureviciene, I., Waselius, T., Tanila, H., and Penttonen, M. (2017). Hippocampal electrical stimulation disrupts associative learning when targeted at dentate spikes. J. Physiol. *595*, 4961–4971.

Pallud, J., Le Van Quyen, M., Bielle, F., Pellegrino, C., Varlet, P., Cresto, N., Baulac, M., Duyckaerts, C., Kourdougli, N., Chazal, G., et al. (2014). Cortical GABAergic excitation contributes to epileptic activities around human glioma. Sci. Transl. Med. *6*, 244ra89.

Pellegrino, C., Gubkina, O., Schaefer, M., Becq, H., Ludwig, A., Mukhtarov, M., Chudotvorova, I., Corby, S., Salyha, Y., Salozhin, S., et al. (2011). Knocking down of the KCC2 in rat hippocampal neurons increases intracellular chloride concentration and compromises neuronal survival. J. Physiol. *589*, 2475–2496.

Puskarjov, M., Ahmad, F., Kaila, K., and Blaesse, P. (2012). Activity-dependent cleavage of the K-Cl cotransporter KCC2 mediated by calcium-activated protease calpain. J. Neurosci. *32*, 11356–11364.

Ramadoss, J., Lunde, E.R., Ouyang, N., Chen, W.J., and Cudd, T.A. (2008). Acid-sensitive channel inhibition prevents fetal alcohol spectrum disorders cerebellar Purkinje cell loss. Am. J. Physiol. Regul. Integr. Comp. Physiol. *295*, R596–R603.

Rivera, C., Voipio, J., Payne, J.A., Ruusuvuori, E., Lahtinen, H., Lamsa, K., Pirvola, U., Saarma, M., and Kaila, K. (1999). The K+/Cl- co-transporter KCC2

renders GABA hyperpolarizing during neuronal maturation. Nature *397*, 251–255.

Rivera, C., Li, H., Thomas-Crusells, J., Lahtinen, H., Viitanen, T., Nanobashvili, A., Kokaia, Z., Airaksinen, M.S., Voipio, J., Kaila, K., and Saarma, M. (2002). BDNF-induced TrkB activation down-regulates the K+-Cl- cotransporter KCC2 and impairs neuronal Cl- extrusion. J. Cell Biol. *159*, 747–752.

Rivera, C., Voipio, J., Thomas-Crusells, J., Li, H., Emri, Z., Sipilä, S., Payne, J.A., Minichiello, L., Saarma, M., and Kaila, K. (2004). Mechanism of activity-dependent downregulation of the neuron-specific K-Cl cotransporter KCC2. J. Neurosci. *24*, 4683–4691.

Roth, B.L. (2016). DREADDs for Neuroscientists. Neuron *89*, 683–694.

Saitsu, H., Watanabe, M., Akita, T., Ohba, C., Sugai, K., Ong, W.P., Shiraishi, H., Yuasa, S., Matsumoto, H., Beng, K.T., et al. (2016). Impaired neuronal KCC2 function by biallelic SLC12A5 mutations in migrating focal seizures and severe developmental delay. Sci. Rep. *6*, 30072.

Sciaky, N., Presley, J., Smith, C., Zaal, K.J., Cole, N., Moreira, J.E., Terasaki, M., Siggia, E., and Lippincott-Schwartz, J. (1997). J. Cell Biol. *139*, 1137–1155.

Seja, P., Schonewille, M., Spitzmaul, G., Badura, A., Klein, I., Rudhard, Y., Wisden, W., Hübner, C.A., De Zeeuw, C.I., and Jentsch, T.J. (2012). Raising cytosolic Cl- in cerebellar granule cells affects their excitability and vestibulo-ocular learning. EMBO J. *31*, 1217–1230.

Sen, A., Martinian, L., Nikolic, M., Walker, M.C., Thom, M., and Sisodiya, S.M. (2007). Increased NKCC1 expression in refractory human epilepsy. Epilepsy Res. *74*, 220–227.

Staley, K.J., and Mody, I. (1992). Shunting of excitatory input to dentate gyrus granule cells by a depolarizing GABAA receptor-mediated postsynaptic conductance. J. Neurophysiol. *68*, 197–212.

Talley, E.M., Solorzano, G., Lei, Q., Kim, D., and Bayliss, D.A. (2001). Cns distribution of members of the two-pore-domain (KCNK) potassium channel family. J. Neurosci. *21*, 7491–7505.

Tang, X., Kim, J., Zhou, L., Wengert, E., Zhang, L., Wu, Z., Carromeu, C., Muotri, A.R., Marchetto, M.C., Gage, F.H., and Chen, G. (2016). KCC2 rescues functional deficits in human neurons derived from patients with Rett syndrome. Proc. Natl. Acad. Sci. USA *113*, 751–756.

Titz, S., Hormuzdi, S., Lewen, A., Monyer, H., and Misgeld, U. (2006). Intracellular acidification in neurons induced by ammonium depends on KCC2 function. Eur. J. Neurosci. *23*, 454–464.

Wang, F., Wang, X., Shapiro, L.A., Cotrina, M.L., Liu, W., Wang, E.W., Gu, S., Wang, W., He, X., Nedergaard, M., and Huang, J.H. (2017). NKCC1 up-regulation contributes to early post-traumatic seizures and increased post-traumatic seizure susceptibility. Brain Struct. Funct. *222*, 1543–1556.

Witter, M.P. (2007). The perforant path: projections from the entorhinal cortex to the dentate gyrus. Prog. Brain Res. *163*, 43–61.

Wright, R., Newey, S.E., Ilie, A., Wefelmeyer, W., Raimondo, J.V., Ginham, R., McIlhinney, R.A.J., and Akerman, C.J. (2017). Neuronal Chloride Regulation via KCC2 Is Modulated through a GABAB Receptor Protein Complex. J. Neurosci. *37*, 5447–5462.

Zhang, H., Dong, H., Cilz, N.I., Kurada, L., Hu, B., Wada, E., Bayliss, D.A., Porter, J.E., and Lei, S. (2016). Neurotensinergic Excitation of Dentate Gyrus Granule Cells via Gαq-Coupled Inhibition of TASK-3 Channels. Cereb. Cortex *26*, 977–990.

Zuzarte, M., Heusser, K., Renigunta, V., Schlichthörl, G., Rinné, S., Wischmeyer, E., Daut, J., Schwappach, B., and Preisig-Müller, R. (2009). Intracellular traffic of the K+ channels TASK-1 and TASK-3: role of N- and C-terminal sorting signals and interaction with 14-3-3 proteins. J. Physiol. *587*, 929–952.

STAR★METHODS

KEY RESOURCES TABLE

REAGENT or RESOURCE	SOURCE	IDENTIFIER
Antibodies		
Rabbit anti-KCC2	Millipore	Cat# 07-432; RRID:AB_310611
Rabbit anti-Task3	Alomone	Cat# APC-044; RRID:AB_2039953
Nonimmune IgG control antibody	Jackson ImmunoResearch	Cat# 011-000-002; RRID:AB_2337117
Goat anti-Task3	Santa Cruz Biotechnology	Cat# sc-11317; RRID:AB_2131233 (discontinued)
Rabbit anti-HA	Cell Signaling Technology	Cat# 3724; RRID:AB_1549585
Mouse anti-HA	Sigma-Aldrich	Cat# H9658; RRID:AB_260092
Mouse anti-Flag M2	Sigma-Aldrich	Cat# F3165; RRID:AB_259529
Rabbit anti-EEA1	Thermofisher	Cat# PA1-063A; RRID:AB_2096819
Rabbit anti-calregulin	Santa Cruz Biotechnology	Cat# sc-11398; RRID:AB_667959 (discontinued)
Mouse anti-CTR433	Michel Bornens, Curie Inst., Paris	Jasmin et al., 1989
Mouse anti-GM130	BD Transduction Laboratories	Cat# 610822; RRID:AB_398141
Mouse anti beta-III tubulin (TuJ1)	R&D Systems	Cat# MAB1195; RRID:AB_357520
DyLight Fluorescent Dye Conjugates 800	Rockland	Cat# 611-145-002; RRID:AB_1660964
Rabbit anti-HA	Cell Signaling Technology	Cat# 3724S; RRID:AB_1549585
Alexa647-conjugated donkey anti-rabbit	Jackson ImmunoResearch	Cat# 711-605-152; RRID:AB_2492288
Cy3-conjugated goat anti-mouse	Jackson ImmunoResearch	Cat# 115-165-206; RRID:AB_2338695
Chicken anti-GFP	Millipore	Cat# AB16901; RRID:AB_90890
Rabbit anti-Prox1	Millipore	Cat# AB5475; RRID:AB_177485
Rabbit anti-Trek2	Alomone	Cat# APC-055; RRID:AB_2040138
Cy3-conjugated goat anti-rabbit	Jackson ImmunoResearch	Cat# 111-165-003; RRID:AB_2338000
FITC-conjugated goat anti-chicken	Jackson ImmunoResearch	Cat# 103-095-155; RRID:AB_2337384
Bacterial and Virus Strains		
Lentivirus U6-shNT-PGK-EGFP-WPRE	UNC Vector Core	Chevy et al., 2015
Lentivirus U6-shKCC2-PGK-EGFP-WPRE	UNC Vector Core	Chevy et al., 2015
AAV2.1-hM4D(Gi)-mCherry	Viral Vector Facility. Univ. Zurich	Cat# v107
AAV2.1-U6-shNT-PGK-EGFP-WPRE	Atlantic Gene Therapy, Nantes	This study
AAV2.1-U6-shKCC2-PGK-EGFP-WPRE	Atlantic Gene Therapy, Nantes	This study
Chemicals, Peptides, and Recombinant Proteins		
Choline chloride	Sigma-Aldrich	Cat# C7017
NBQX disodium salt	HelloBio	Cat# HB0443
D-AP5	HelloBio	Cat# HB0225
Tetrodotoxin (TTX)	Latoxan	Cat# L8503
Picrotoxin	HelloBio	Cat# HB0506
Gramicidin	Sigma-Aldrich	Cat# G5002
RubiGABA	Abcam	Cat# ab120409
CGP54626	Tocris Bioscience	Cat# 1088
Bicuculline methochloride	HelloBio	Cat# HB0895
Valium 10mg/2ml (Diazepam)	Roche (Centravet)	N/A
Ketamine 1000	Virbac (Centravet)	N/A
Rompun 2% (Xylazine)	Bayer (Centravet)	N/A

(*Continued on next page*)

Continued

REAGENT or RESOURCE	SOURCE	IDENTIFIER
Vetergesic 0.3mg/ml (Buprenorphine)	Ceva (Centravet)	N/A
Pilocarpine hydrochloride	Sigma-Aldrich	Cat# P6503
Lithium Chloride	Sigma-Aldrich	Cat# L4408
(-) Scopolamine methyl nitrate	Sigma-Aldrich	Cat# S2250
Clozapine N-oxide	HelloBio	Cat# HB1807
Normal goat serum	FisherScientific	Cat# 11530526
DMEM GlutaMAX (Neuro2a)	FisherScientific	Cat #10567014
DMEM GlutaMAX (HEK)	FisherScientific	Cat #41965039
Fetal bovine serum	FisherScientific	Cat# 15377636
Transfectin	BioRad	Cat# 1703350
Trypsine	FisherScientific	Cat# 11580626
Hank's Balanced Salt Solution	FisherScientific	Cat# 11570476
Minimum Essential Medium	FisherScientific	Cat# 11550556
Horse serum	FisherScientific	Cat# 10368902
L-glutamine	FisherScientific	Cat# 11500626
Sodium Pyruvate (100 mM)	FisherScientific	Cat# 11530396
Neurobasal	FisherScientific	Cat# 11570556
B27 supplement	FisherScientific	Cat# 11530536
Penicillin/streptomycin	FisherScientific	Cat# 11548876
HEPES Buffer 1M	Sigma-Aldrich	Cat# 11560496
Poly-ornithine	Sigma-Aldrich	Cat# P8638
Critical Commercial Assays		
Pierce BCA protein assay	Thermofisher	Cat# 23225
Dynabeads Protein G	Thermofisher	Cat# 10003D
NuPage Novex 4-12% Bis-Tris Gel	FisherScientific	Cat# 10247002
HA-Tag (C29F4) Rabbit mAb beads	Cell Signaling Technology	Cat# 3956S
EZview Red ANTI-FLAG M2 Affinity Gel	Sigma-Aldrich	Cat# F2426
GE Healthcare Amersham Protran NC Nitrocellulose Membrane	FisherScientific	Cat# 10600002
16 channel linear silicon probes	Neuronexus	Cat# A1x16-5mm-100-413-CM16LP
Borosilicate glass capillaries	Hilgenberg GmbH	Cat# 1404513
Tungsten bipolar electrodes	World Precision Instruments	Cat# TST33A05KT
Protease inhibitors	Sigma-Aldrich	Cat# 11697498001
Experimental Models: Cell Lines		
Neuro2a	DSMZ GmbH	Cat# ACC148 (batch #8)
HEK293	ATCC	Cat# CRL-1573
Experimental Models: Organisms/Strains		
Rat: Male wild-type Sprague Dawley	Janvier Labs	N/A
Recombinant DNA		
Flag-tagged rat full-length KCC2	Our lab	Chamma et al., 2013
HA-tagged mouse Task3	G. Sandoz, Nice Univ.	Levitz et al., 2016
HA-EGFP-HaloTag2	Addgene	Cat# 41742
pCAG empty vector	L. Maroteaux, IFM, Paris. Based on Addgene Cat# 89684	N/A
pGeneClip U6shRNA NT-PGK-EGFP	Our lab	Gauvain et al., 2011
pGeneClip U6shRNA KCC2-PGK-EGFP	Our lab	Gauvain et al., 2011
P58-GFP	J Lippincott-Schwartz, Janelia Campus	Sciaky et al., 1997
GalTase-GFP	J Lippincott-Schwartz, Janelia Campus	Sciaky et al., 1997
pEGFP-GalT	Addgene	Cat# 11929

LEAD CONTACT AND MATERIALS AVAILABILITY

Further information and requests for resources and reagents should be directed to and will be fulfilled by the Lead Contact, Jean Christophe Poncer (jean-christophe.poncer@inserm.fr).

EXPERIMENTAL MODEL AND SUBJECT DETAILS

Animals
Juvenile male Wistar rats were obtained from Janvier Labs (Le Genest Saint Isle, France). All procedures conformed to the International Guidelines on the ethical use of animals, the French Agriculture and Forestry Ministry guidelines for handling animals (decree 87849, license A 75-05-22) and were approved by the Charles Darwin ethical committee (APAFIS2015111011588776v3).

HEK293 and Neuro-2a cultures
HEK293 and Neuro-2a cells were grown in DMEM GlutaMAX (Invitrogen) supplemented respectively with glucose and fetal bovine serum (5 g/l and 10% for HEK293 cells and 1g/l and 10% for Neuro-2a cells, respectively). Cells (60%–70% confluent) were co-transfected using Transfectin (BioRad) according to the manufacturer's instructions.

Primary hippocampal cultures
Primary cultures of hippocampal neurons were prepared as previously described (Gauvain et al., 2011). In brief, hippocampi were dissected from embryonic day 18-19 Sprague-Dawley rats and trypsinized (0.25% v/v) and mechanically dissociated in Hank's Balanced Salt Solution containing buffered with HEPES (10 mM). Neurons were plated at a density of 120.10^3 cells/ml onto 18-mm glass coverslips pre-coated with poly-ornithine (50 μg/ml). The plating medium was prepared with Minimum Essential Medium supplemented with 10% horse serum, L-glutamine (2 mM) and sodium pyruvate (1 mM). Cells were allowed to attach for 3-4 h at 37°C in a 5% CO2 humidified incubator before replacing the medium with Neurobasal supplemented with B27, L-glutamine (2 mM) penicillin/streptomycin (200 units/ml and 200 μg/ml, respectively). Culture medium was supplemented with 20% fresh medium every week. Hippocampal cultures were infected at 15–17 DIV using lentiviral vectors described below, using 500 nl/ml of purified virus solution. Cultures were washed twice in ice-cold PBS and lysed in lysis buffer (25 mM Tris-HCl, pH 7.4, 250 Mm NaCl, 50 mM NaF, 5 mM PPi, 5 mM EDTA, 5 mM EGTA, 1 mM sodium orthovanadate, 1% Triton-X, and protease inhibitor mixture; Roche).

After 15 min centrifugation at 14000 g, supernatants were mixed with Laemmli sample buffer and boiled at 95°C for 5 min. Samples were subjected to standard SDS-PAGE and transferred to nitrocellulose membranes. Blots were probed with rabbit KCC2 and mouse neuron-specific beta-III tubulin (TuJ1) antibodies, and fluorescent secondary antibodies (DyLight 800) using Odyssey infrared imaging system (LI-COR Bioscience). For quantification, all data were normalized to internal TuJ1 control signals.

METHOD DETAILS

Virus and constructs
Rat SLC12A5-specific and non-target shRNA sequences (Gauvain et al., 2011) were introduced in pTrip vector under U6 promoter and used to produce purified lentiviral particles (titer 7-9 × 10^9 TU/ml, UNC Vector Core Facility) (Chevy et al., 2015). For some experiments, these same sequences were introduced in pAAV vector under U6 promoter and used to produce purified AAV particles (AAV2.1-shRNA-GFP, titer 10^{13} TU/ml, Atlantic Gene Therapy, Nantes). AAV particles expressing inhibitory DREADD under synapsin promoter were obtained from the Viral Vector Facility of Zurich University (AAV2.1-hM4D(Gi)-mCherry, titer 10^{13} TU/ml).

Stereotaxic viral injection and EcoG electrode implantation

30-days Wistar rats were anesthetized by intraperitoneal injection of ketamine / xylazine (75/10 mg/kg) and subcutaneous injection of buprenorphine (0.05 mg/kg) for analgesia. Animals were then head-fixed in a stereotaxic apparatus. 1 μl of lentivirus (concentrated at 10^9 TU/ml) was injected bilaterally in the dentate gyrus (AP −4.0 mm, ML ± 2.5 mm, DV −3.1 mm) at 125 nl/min. For DREADD experiments, 500nL of mix AAV2.1-shRNA-GFP and AAV2.1-hM4D(Gi)-mCherry (ratio 2/3:1/3) was injected bilaterally in the dentate gyrus. For experiments in CA1, animals were injected bilaterally with 1 μl of AAV2.1-shRNA-GFP (AP −4.0 mm, ML ± 2.5 mm, DV −2.35 mm).

For pilocarpine experiments, animals were also implanted with EcoG electrodes soldered to stainless steel screws. Two electrodes were placed above each hippocampus, at the same coordinates as the injection sites. A third screw was placed above the cerebellum and used as reference.

Intracerebral probe implantation

For intra-hippocampal recordings, animals were anesthetized with isoflurane one week following viral injection, and injected subcutaneously with 0.05 mg/kg of buprenorphine for analgesia. One 16-channels silicon probe was implanted in the right hemisphere, at the site of the injection. Signals were monitored during the insertion of the probe to ensure correct localization of the probe in the hippocampus. One stainless steel screw was placed above the cerebellum and connected to the probe as a reference. Four additional screws were placed above the prefrontal cortex and the contralateral hemisphere to secure the dental cement adhesion. During the recovery period (minimum 3 days), rats were daily monitored and additional injection of buprenorphine (subcutaneous, 0.05 mg/kg) were made in case of detectable pain.

Electrophysiology

Slice preparation

10 to 20 days after viral injection, animals were deeply anesthetized with ketamine / xylazine (115/15 mg/kg) and transcardially perfused with an ice-cold choline-based solution containing (in mM): 110 Choline Cl, 25 Glucose, 25 $NaHCO_3$, 11.6 Ascorbic acid, 3.1 Pyruvic acid, 1.25 NaH_2PO_4, 2.5 KCl, 0.5 $CaCl_2$, 7 $MgCl_2$ saturated with 95% O_2/5% CO_2. Rats were then decapitated, hippocampi were rapidly dissected and 400μm transverse sections were prepared using a vibratome (Microm, Thermofisher). Slices were then transferred and allowed to recover for 1 hour in a humidified interface chamber filled with bicarbonate-buffered ACSF pre-heated at 37°C and oxygenated with 5% CO_2 in O_2, containing (in mM): 126 NaCl, 26 $NaHCO_3$, 10 Glucose, 3.5 KCl, 1.25 NaH_2PO_4, 1.6 $CaCl_2$, 1.2 $MgCl_2$. For recordings, slices were transferred in a submerged recording chamber and superfused with ACSF maintained at 32°C.

Patch clamp recordings

Electrophysiological recordings were made with 4-5 MΩ borosilicate glass pipettes. Signals were acquired with a Multiclamp 700B amplifier (Molecular Devices), low-pass filtered at 10 kHz, and digitized at 20 kHz. All cells were recorded in the suprapyramidal blade of the dentate gyrus.

For perforated-patch recordings, internal solution contained (in mM) 140 KCl and 10 HEPES (pH adjusted to 7.4 with KOH). Gramicidin was added in the pipette solution to reach a concentration of 60 μg/ml. Rubi-GABA (15 μM) was added in ACSF together with NBQX (20 μM), APV (50 μM), CGP54626 (10 μM) and TTX (1 μM). Rubi-GABA was photolyzed using a digital modulated diode laser beam at 405 nm (Omicron Deepstar, Photon Lines) delivered through a single path photolysis head (Prairie Technologies). The laser beam diameter was set to a diameter of 3-5 μm and was directed onto the soma of the recorded neuron. Photolysis was induced by a 5 ms/30 mW pulse. Once access resistance was stabilized, cells were held at a potential of −70 mV and 3.5 s voltage steps ranging from −100 to −30 mV were applied to the cell. Laser pulses were delivered at 2.2 s after the onset of the voltage step to allow for stabilization of the holding current. Currents were analyzed offline using Clampfit software. Voltages were corrected for liquid junction potential (4.1 mV) and for the voltage drop through the series resistance and E_{GABA} was derived from a linear regression of the I/V curve over the 4 data points around current reversal.

For all other patch clamp experiments, cells were recorded in whole-cell configuration and maintained at −70 mV. All voltages were corrected offline for liquid junction potential (of 14.5 mV).

Intrinsic properties were evaluated using an internal solution containing (in mM) 120 K-Gluconate, 10 KCl, 10 HEPES, 0.1 EGTA, 4 $MgATP$, 0.4 Na_3GTP (pH adjusted to 7.4 with KOH) and blocking synaptic transmission with NBQX, APV and picrotoxin (10μM). Resting membrane potential was measured using I = 0 current clamp mode one minute after break-in. Input resistance was measured in current-clamp mode with −50 pA current steps. Input-output curves were generated by plotting firing frequency in response to either series of 800 ms current steps (ranging from −100 to 375 pA, 25 pA step increment, Figures 2C and S3D) or multiples of synaptic current waveforms (Figure 4C). For potassium currents measurements, recorded from either granule cells (Figures 2G and 2H) or Neuro-2a cells expressing mGFP, HA-tagged mouse Task-3 with or without Flag-tagged rat KCC2 (ratio: 1/3/6; Figure 3F), TTX (1 μM) was added to the bath. Currents were recorded in voltage-clamp mode between −120 mV and −60 mV with a continuous ramp at 0.03 mV/ms. Conductance of Task-3 mediated currents were then derived from a linear regression of the last 500 ms of the outward currents. For EPSP/spike coupling recordings, artificial waveforms derived from mEPSC recordings were used as a current command applied to the patch pipette. Effect of CNO application on membrane potential was estimated by whole-cell recordings in current-clamp mode with no current injection.

For miniature excitatory postsynaptic current (mEPSCs) recordings, pipettes were filled with internal solution containing (in mM) 115 Cs-Methylsulfonate, 20 CsCl, 10 HEPES, 0.1 EGTA, 4 MgATP, 0.4 Na$_3$GTP (pH adjusted to 7.4 with CsOH) and currents were isolated by adding TTX and bicuculline methochloride (20 μM) to the extracellular solution. For miniature inhibitory postsynaptic currents (mIPSCs), pipettes were filled with (in mM) 135 CsCl, 10 HEPES, 10 EGTA, 4 MgATP, 0.4 Na$_3$GTP, 1.8 MgCl$_2$ (pH adjusted to 7.4 with CsOH) and currents were isolated by adding TTX, NBQX and APV in the bath. Series and input resistance were regularly monitored with −5 mV voltage steps and recordings were interrupted if either value varied by more than 20 %. Miniature synaptic currents were detected and analyzed offline using Detectivent software (Ankri et al., 1994).

Extracellular field recordings

For extracellular recordings, a recording pipette of 2-3 MΩ resistance was filled with ACSF and inserted within the granular layer, in a densely infected area of the dentate gyrus. A tungsten bipolar electrode (0.5 MΩ) was used to stimulate perforant path inputs. Stimulation intensity was adjusted to induce a population spike of about half its maximum amplitude. Field EPSP (fEPSP) slope was determined over a 1ms window preceding the population spike. Population spike amplitude was assessed as the distance between its peak and the baseline extrapolated from its initiation and termination points using a routine written under MATLAB.

Biochemistry

Co-immunoprecipitation assays from rat hippocampal homogenates

Hippocampi were dissected from adult Sprague Dawley female rats and homogenized by sonication in co-immunoprecipitation buffer (1 ml/100 mg of tissue) and solubilized by rotation for 2 to 4 hours at 4°C. After centrifugation at 20,000 g for 40 minutes at 4°C, protein content of the supernatant was measured by BCA protein assay (Pierce). 6.5 mg of proteins were transferred into microtube and 5 μg of primary antibody (Rabbit anti-KCC2, Millipore, and Rabbit anti-Task-3, Alomone) or nonimmune IgG control antibody of the same species (Jackson Immunoresearch) were added. Samples were then incubated overnight at 4°C under rotation. Complexes were precipitated with 20 μl protein-G magnetic beads (Invitrogen) for 2 hours at 4°C. Beads were then washed twice with 1ml of co-immunoprecipitation buffer and once with triton-free co-immunoprecipitation buffer. Bound complexes were eluted in 4X sample buffer (Invitrogen) for 1 hour at 37°C. Samples were analyzed by SDS-PAGE and western blot.

Co-immunoprecipitation assays from HEK293 cells

HEK293 cells were grown in DMEM GlutaMAX (Invitrogen) supplemented with 5 g/l glucose and 10% fetal bovine serum. Cells (60%–70% confluent) were co-transfected using transfectin according to the manufacturer's instructions with plasmids expressing Flag-tagged rat KCC2 (Chamma et al., 2013) and HA-tagged mouse Task-3 (kindly provided by Guillaume Sandoz, Nice Univ., France) or HA-tagged GFP (Addgene) as control (with a 1:1 ratio). 48 hours after transfection, cells were homogenized by sonication in co-immunoprecipitation buffer containing (in mM): 50 Tris-HCl pH 7.4, 150 NaCl, 1 EDTA, as well as 0.5% Triton X-100 and protease inhibitors. Cells were then solubilized by rotation for 2 hours at 4°C and centrifuged at 20,000 g for 30 minutes at 4°C. Supernatants were transferred into a microtube with 20 μl of pre washed HA-Tag (C29F4) Rabbit mAb beads (Cell Signaling Technology) or EZview Red Anti-FLAG M2 Affinity Gel (Sigma-Aldrich). Samples were incubated overnight at 4°C under rotation and processed as above.

Western blotting

Proteins were separated on a 4%–12% SDS polyacrylamide gradient gel (Invitrogen) and transferred onto a nitrocellulose membrane (GE Healthcare). For co-immunoprecipitation assays from rat hippocampal homogenate, blots were probed with antibodies against KCC2 (rabbit, 1/1000, Merck-Millipore) and Task-3 (goat, 1/250, Santa Cruz). This Task-3 antibody has been previously validated in western blots from Task-3 KO mice (Zhang et al., 2016). For co-immunoprecipitation assays from HEK293 cells, blots were probed with HA (mouse, 1/3000, Cell Signaling Technology) and KCC2 (rabbit, 1/1000, Merck-Millipore) or FlagM2 (mouse, 1/1000, Sigma-Aldrich). The primary antibodies were detected with fluorescent secondary antibodies (1/1000-1/3000, DyLight 700 or 800, Rockland) using Odyssey infrared imaging system (LI-COR Bioscience). All biochemical assays were repeated at least 3 times on independent hippocampal extracts or cultures.

Immunocytochemistry

Neuro-2a cells were grown on glass coverslips in DMEM GlutaMAX (Invitrogen) supplemented with 1 g/l glucose and 10% fetal bovine serum. Cells at 60%–70% confluence were co-transfected using Transfectin according to manufacturer's instructions with plasmids expressing HA-tagged mouse Task-3 and either Flag-tagged rat KCC2 (Chamma et al., 2013; Heubl et al., 2017) or a pCAG empty vector as control (with a 1:3 ratio, Figures 3D and 3E). For identification of some subcellular compartments (Figures 3G and 3H), cells were co-transfected with plasmids expressing HA-tagged mouse Task-3 and either p58-GFP or GalTase GFP (kindly provided by Jennifer Lippincott-Schwartz, Janelia Research Campus) with a 1:1 ratio. 48 hours after transfection, cells were washed with PBS, fixed with paraformaldehyde (4%) supplemented with 4% sucrose in PBS and permeabilized with 0.25% Triton X-100 in PBS. After 3 × 10 min washes in PBS, cells were incubated for 30 min in blocking buffer (10% normal goat serum in PBS). Incubation with primary antibodies including HA (rabbit, 1/2000, Chemicon; or mouse, 1/250, Sigma), FlagM2 (mouse, 1/2000, Sigma), CTR433 (mouse, 1/250), Calregulin (rabbit, 1/250, Santa Cruz Biotechnology), EEA1 (rabbit, 1/250, Thermofisher), GM130 (mouse, 1/250, BD Transduction Laboratories) was then performed in blocking buffer for 2 hours at room temperature. After 3 × 10 min washes in PBS, cells were incubated with secondary antibodies for 1 hour (goat anti-rabbit Alexa CY3, goat anti-mouse Alexa CY3, donkey anti-mouse Alexa 647, donkey anti-rabbit Alexa CY3, 1/1000, donkey anti-rabbit Alexa

647, 1/1000 and goat anti-mouse CY3, 1/2000, all from Jackson Immunoresearch). Coverslips were washed 3 times in PBS and mounted in Mowiol/Dabco (25 mg/ml) solution. Stacks (z-step: 0.29 μm) of immunofluorescence images were acquired using an upright confocal microscope (Leica TCS SP5), using a 63x 1.40-N.A. objective and lasers set at 488, 561 and 633 nm for excitation of GFP, Cy3 and Alexa 647, respectively.

Colocalization analysis (Figures 3G and 3H) was performed from 3D images using Imaris (Bitplane) colocalization tool. In brief, individual transfected cells were isolated from 3D stacks using either automatic or manual surface-based masks. Cytofluorograms were then constructed using Imaris colocalization tool and a threshold was set manually for each channel. "Colocalization index" was then computed as the percentage of suprathreshold material (integrated intensity) of HA-Task-3 immunofluorescence channel localized within suprathreshold voxels of immunofluorescent signal corresponding to each subcellular marker.

Immunohistochemistry

At least 2 weeks following viral injections, rats were anesthetized by intraperitoneal ketamine/xylazine injection (110/15 mg/kg) and perfused transcardially with ice-cold cutting solution of choline as above. Brain were removed, postfixed in PFA 4% for 48 hours and stored at 4°C in 30% sucrose PBS. Parasagittal sections (40 μm thick) were obtained using a cryotome. After washes, brain slices were preincubated 3 hours with 0.5% Triton and 10% goat serum in PBS and then 48 hours at 4°C with primary antibodies: GFP (chicken, 1:1000, Millipore), KCC2 (rabbit, 1:400, Millipore), Prox1 (rabbit, 1:10000, Millipore), Task-3 (rabbit, 1:400, Alomone), Trek-2 (rabbit, 1:400, Alomone). After rinsing in PBS, slices were incubated 3 hours with secondary antibody (Cy3-coupled goat anti-rabbit and FITC-coupled goat anti-chicken) and mounted with Mowiol/Dabco (25 mg/mL). Images were acquired on an upright confocal microscope (Leica TCS SP5), using a 63X 1.40-N.A. objective with 2X electronic magnification and lasers set at 488 and 561 nm for excitation of FITC and Cy3, respectively. Stacks of 4 to 6 μm, 0.2 μm apart, optical sections were acquired. For images of the entire dentate gyrus, images were acquired using a 10X objective and stacks of 10 to 20 μm optical sections.

Behavior and recordings

All recordings took place in a dimly lit area enclosed by black curtains. Animals were handled for at least 3 days for habituation and to ensure stability of the recordings (location of the probe, power of the signal) before experiments started. A 80 cm x 80 cm arena with 50 cm high black plastic walls was used for exploration phase. A white card on one of the wall was used as spatial cue. For sleep recordings, animals were put in a white cylinder box (20 cm of diameter, 40 cm high). During the habituation phase, animals were placed in the cylinder box then in the empty arena for 10 min each, twice a day.

For recordings of awake behavior, new objects were placed in the open-field to stimulate exploration. All sleep recording sessions took place during the 2 hours following exploration of novel objects. For DREADD experiments, saline or CNO (1 mg/kg) was injected in i.p. 30 minutes before starting recording. All recordings took place less than 3 hours after i.p. injection.

Data were acquired at 20 kHz using an Intan recording controller (Intan Technologies) and Intan Recording Controller software (version 2.05).

Data analysis

All analyses were performed offline using MATLAB built-in functions and custom-written scripts as well as Chronux (http://chronux.org/) and the FMAToolbox (http://fmatoolbox.sourceforge.net/). Power spectra and spectrograms were computed using multi-tapers estimates on the raw LFP. Theta power was determined in the 5–10 Hz band. Dentate spikes detection was performed after high-pass filtering (> 30Hz), squaring and normalizing the field potential in the dentate gyrus. DS were defined as events of positive deflection peaking at > 8 s.d. and remaining above 4 s.d. for less than 30 ms. Current source density analysis (CSD) revealed two distinct DS profiles, previously described as DS1 and DS2 (Bragin et al., 1995). Since most (70%–80%) DS in our recording conditions were of type 2, we did not further attempt to distinguish between DS subtypes in our analysis.

Ripple detection was performed by band-pass filtering (100–600 Hz), squaring and normalizing, followed by thresholding of the field potential recorded in CA1 pyramidal layer. SPW-Rs were defined as events starting at 4 s.d., peaking at > 6 s.d., and remaining at > 4 s.d. for < 150 ms and > 15 ms

Electrocorticogram (EcoG) recordings and epilepsy induction

EcoG data were acquired at 20 kHz using Epoch Wireless recording system (Ripple) and Clampex software (Molecular Devices). Video recording (29 frames/s) was synchronized to data acquisition to enable offline analysis.

For epilepsy induction, animals received intraperitoneal injection of 127 mg/kg of lithium chloride 18 hours before treatment. The following day, animals received i.p. injection of 1 mg/kg of methylscopolamine in order to prevent peripheral effects of pilocarpine. 30 min later, 40 mg/kg of pilocarpine was injected i.p. Both video and EcoG data were acquired for one hour following pilocarpine injection. Status epilepticus was then interrupted by i.p. injection of 5 mg/kg diazepam. Animals were then sacrificed and brain were recovered and processed for visualization of the infected area.

Rat behavior was scored according to the following modified Racine's scale: stage 1, immobility and chewing; stage 2, neck and body clonus; stage 3, forelimb clonus and rearing; stage 4, *status epilepticus*, uninterrupted seizures. The onset of *status epilepticus* was assessed based on EcoG recordings.

QUANTIFICATION AND STATISTICAL ANALYSIS

Statistics

All statistical tests were performed using MATLAB functions (Statistics and Machine Learning Toolbox). Data are presented as mean ± sem unless stated otherwise. All tests are two-tailed tests. Comparison of means was performed using Student's t test for normally distributed variables (tested with Shapiro-Wilk test) of equal variances (tested with Bartlett test). Otherwise, comparison was performed using the non-parametric Mann-Whitney test. Kolmogorov-Smirnov test was used for comparison of distributions. Significance was determined as $p < 0.05$. Repeats for experiments and statistical tests carried out are indicated in the figure legends and in the main text, respectively.

Supplemental Information

KCC2 Regulates Neuronal Excitability

and Hippocampal Activity via Interaction

with Task-3 Channels

Marie Goutierre, Sana Al Awabdh, Florian Donneger, Emeline François, Daniel Gomez-Dominguez, Theano Irinopoulou, Liset Menendez de la Prida, and Jean Christophe Poncer
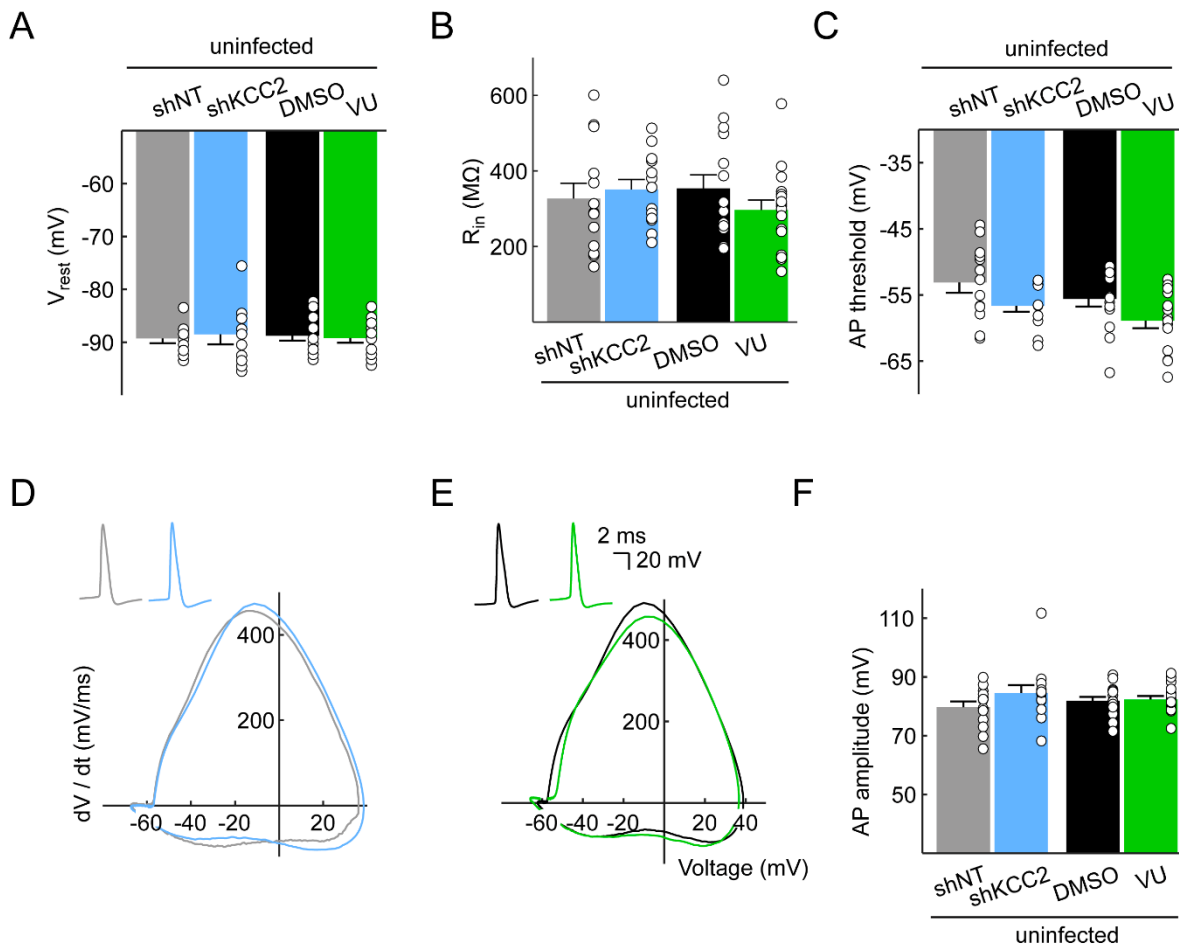
Supplementary figures

Figure S1. Increased excitability upon KCC2 knockdown is cell-autonomous and independent of KCC2-mediated ion transport *(related to Figure 1).*

Membrane and spike properties were analyzed for uninfected cells from slices infected with lentiviral vectors expressing non-target (grey, n=13 cells, 5 rats) or KCC2-directed (light blue, n=13 cells, 7 rats) shRNA sequences. Effect of KCC2 blockade for >30 min with its specific antagonist VU0463271 was also analyzed (green, n=17 cells, 5 rats) and compared to DMSO treatment (black, n=15 cells, 4 rats) in slices from control, non-infected rats. No differences were observed in membrane potential (**A,** shNT *vs* shKCC2 p=0.83, DMSO *vs* VU p=0.75), input resistance (**B,** shNT *vs* shKCC2 p=0.63, DMSO *vs* VU p=0.20) as well as AP threshold (**C,** shNT *vs* shKCC2 p=0.063, DMSO *vs* VU p=0.055), waveform (**D-E**) and amplitude (**F,** shNT *vs* shKCC2 p=0.24, DMSO *vs* VU p=0.77).
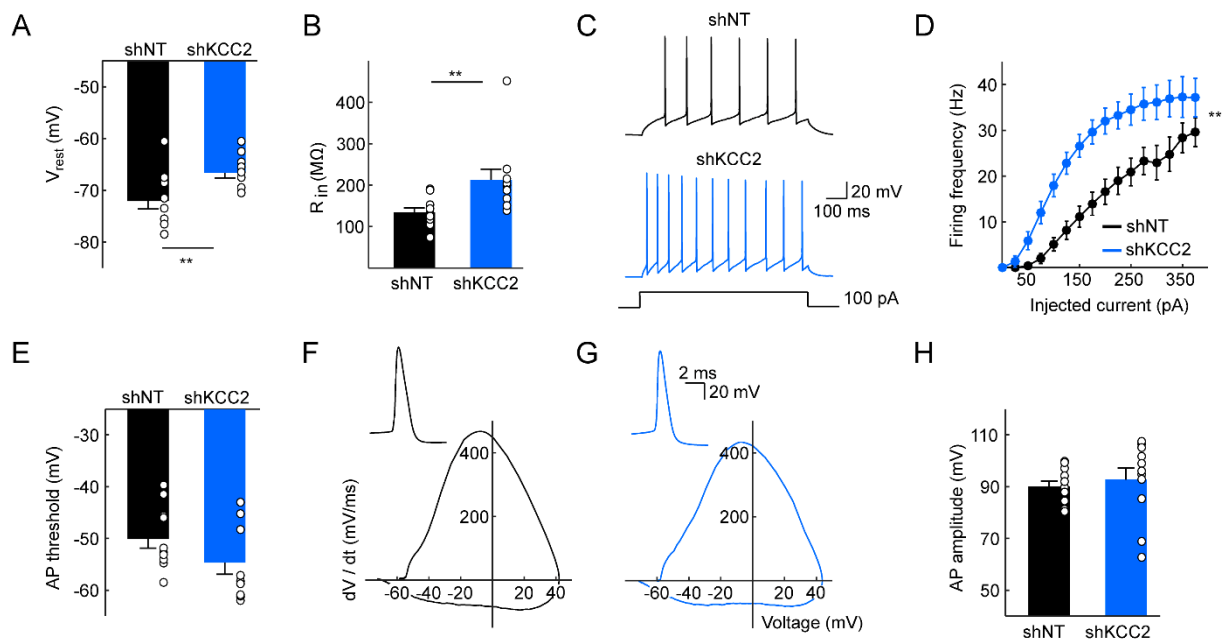
Figure S2. Increased excitability in CA1 pyramidal cells upon KCC2 suppression
(related to Figure 1).

A-B, Membrane properties of CA1 superficial pyramidal cells expressing non-target (n=11 cells, 3 rats) or KCC2-directed (n=11 cells, 3 rats) shRNA, as detected in whole-cell patch clamp recordings while blocking synaptic transmission. KCC2 knockdown resulted in depolarized membrane potential (A) and increased input resistance (B). **C,** Individual traces in both conditions for a depolarizing current pulse of 100 pA. **D,** Mean input/output relationships representing the frequency of APs as a function of injected current. No difference was observed between shNT and shKCC2-expressing CA1 pyramidal cells with regard to action potential threshold (**E**, p=0.13), spike waveform (**F-G**) or spike amplitude (**H**, p=0.59). **p<0.01.

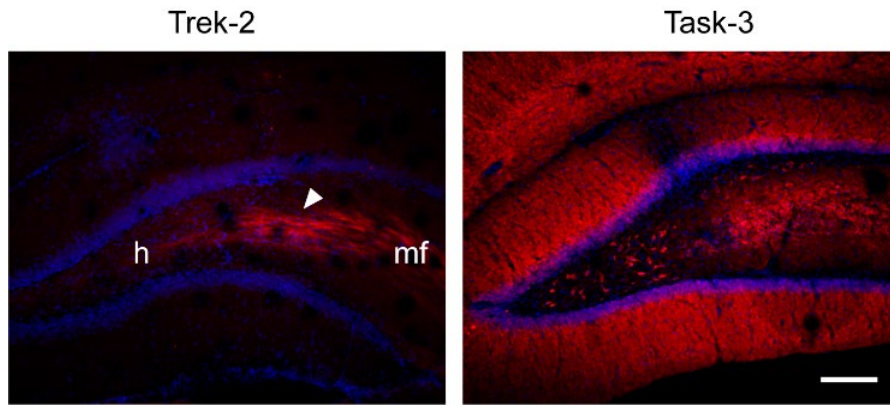**Figure S3. Differential subcellular localization of leak-potassium channels in the dentate gyrus** *(related to Figure 3).*

Left, Average intensity projection of confocal micrographs of dentate gyrus immunostained with Trek-2 antibody. Note the massive expression of Trek-2 in mossy fibers (arrowhead) and its relative absence in the granular and molecular layers of the dentate gyrus. h : hilus, mf : mossy fibers. Right, Average intensity projection of confocal micrographs of dentate gyrus immunostained with Task-3 antibody revealing a strong expression in both granular and molecular layers as well as in hilar mossy cells. Scale, 200 µm.
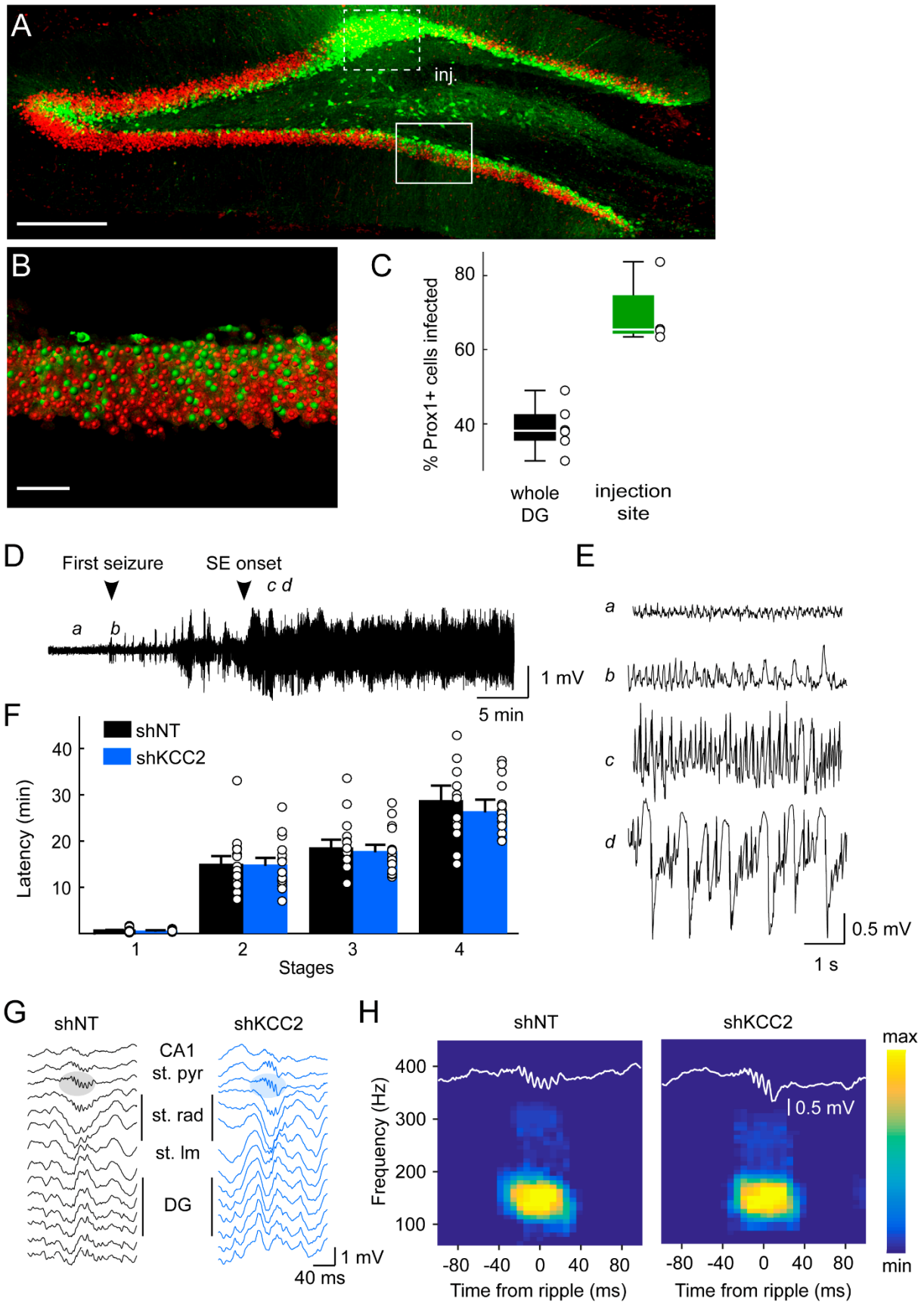
Figure S4. KCC2 suppression in the dentate gyrus does not induce or promote epileptiform activity *(related to Figure 5).*

A, Maximum intensity projection of confocal micrographs showing infected cells (GFP, green) and Prox1 (red) immunostaining in a parasagittal hippocampal slice 2 weeks after lentivirus injection. Dotted box: injection site. Scale, 300 µm. **B,** Imaris 3D rendering of plain boxed area shown in A. For colocalization estimates, dentate granule cell nuclei were automatically detected based on Prox1 immunostaining (red spheres) while infected cells were detected based on GFP fluorescence (green spheres). **C,** Summary of mean infection rate through the whole dentate gyrus (n=6 slices, 3 animals) and within 250 µm around the infection site (n=4 slices, 2 animals). **D,** Example trace of an EcoG recording during epilepsy induction with a pilocarpine protocol. Arrowheads indicate the timing of the first seizure and the onset of the *status epilepticus*. **E,** Expanded sections of the recording shown in A, showing the evolution of the EcoG signal at different time points of ictogenesis. **F,** Behavioral state was classified according to modified Racine's scale as follows: stage 1, immobility and chewing; stage 2, neck and body clonus; stage 3, forelimb clonus and rearing; stage 4, *status epilepticus*, uninterrupted seizures. The onset of *status epilepticus* was assessed based on EcoG recordings. Latency to different stages was similar between groups (n=15 animals each). **G,** Traces of ripple events recorded in CA1 during sleep for rats implanted with 16-channels silicon probes as in Fig. 5. **H,** Ripples were automatically detected and 100 events per animal were randomly selected (shNT n=5 rats, shKCC2 n=7 rats). Suppression of KCC2 in the dentate gyrus did not lead to pathological fast ripples as evidenced by the absence of band around 300 Hz in the average time-frequency spectra.
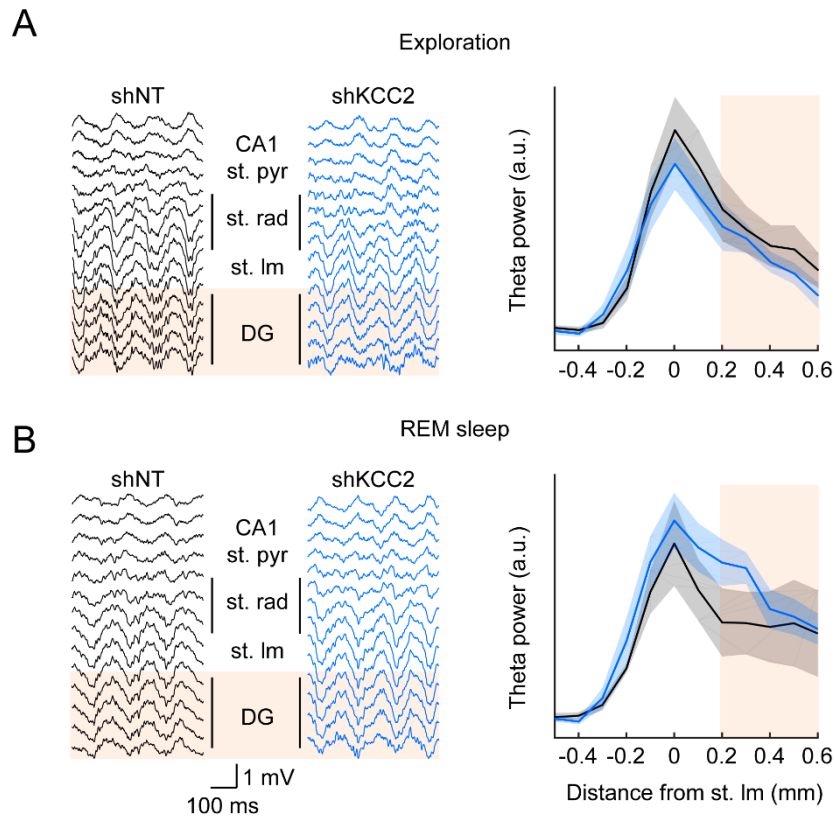
Figure S5. KCC2 suppression in the dentate gyrus does not affect hippocampal theta rhythm *(related to Figure 5).*

A, Left, 500 ms stretches of intrahippocampal recordings (as in Fig. 5) during exploratory behavior in rats expressing non-target shRNA (left, black) or KCC2-directed shRNA (blue, right) in the dentate gyrus. Note the prominent theta oscillation in all channels. The localization of the *stratum lacunosum moleculare* was defined by the highest power of theta and CA1 was identified by the presence of action potentials and of ripples during sleep. Localization of the dentate gyrus is highlighted in orange. Right, theta power in the 5-10 Hz frequency band measured over >1 min of recording using multi-tapers estimates. Power (in arbitrary units, a.u.) is represented as a function of the electrode localization. Depth of the electrode is expressed as the distance from *stratum lacunosum moleculare* (SLM). (2-way ANOVA, $F_{11,144}=2.03$, p=0.15). **B,** Similar as A, but during REM sleep. Depth profile was slightly different between groups (2-way ANOVA, $F_{11,133}=5.96$, p=0.016). However, comparisons for each layer individually did not yield any significant difference (Mann-Whitney, p>0.05 for all layers).